UNIVERSIDAD DE CONCEPCIÓN
FACULTAD DE CIENCIAS FÍSICAS Y MATEMÁTICAS

CHARACTERIZING THE MOLECULAR GAS IN THE SMALL MAGELLANIC CLOUD

With different carbon transitions

Por: Karla Rodriguez Ambler

Tesis presentada a la Facultad de Ciencias Físicas y Matemáticas de la Universidad de Concepción para optar al grado académico de Magíster en Astronomía

Junio 2026
Concepción, Chile

Profesor guía: PhD. Rodrigo Herrera-Camus
Profesora co-guía: PhD. Mónica Rúbio

To Enrique, who always supported my dreams and celebrated them as his own.

AGRADECIMIENTOS

Quiero agradecer a Almendra, mi hermana, por ser la primera en creer siempre en mí, acompañarme, enseñarme y darme el ejemplo de lo que significa ser una estudiante integral; a Viviana y Carlos, mis padres, por darme el apoyo para estudiar una carrera poco tradicional y por entregarme los valores necesarios para terminar con éxito una etapa tan importante y complicada como lo es el posgrado; y a Mario, mi padrastro, por brindarme siempre su amparo incondicional. También creo necesario mencionar especialmente a mi profesor guía, Rodrigo, por recibirme y orientarme siempre con una sonrisa, por creer en mi potencial y, más aún, por hacer que yo misma creyera en él, y sobre todo por mostrarme la profesional que quiero ser; y a mi profesora co-guía, Mónica, por acogerme en su tutela con un toque maternal, por estar siempre atenta a mi proceso de aprendizaje y crecimiento académico, y por ser un referente de cómo, siendo mujer, es posible alcanzar el éxito independientemente de las presiones y estigmas que una debe enfrentar en un área como la astronomía.

No puedo dejar de agradecer a mis amigos Aníbal, Leo, Lucas, Agus, Camilo, Mellado, Evángelo y Scarllet, por celebrarme cada logro, e incluso derrota, por escucharme siempre y tratar de apoyarme a pesar de pertenecer a otras áreas, además de regalarme tantos momentos de risa y felicidad dentro del estrés que puede llegar a significar terminar una carrera científica. Me gustaría además, agradecer a Amaru, quien me mostró que se puede ser un excelente profesional, sin perder lo que realmente nos hace a nosotros mismos.

Finalmente, quisiera agradecer a Enrique, mi esposo, por estar a mi lado en cada momento en que la carrera me desafió, sin importar el ámbito en que fuera; por impulsarme a seguir, cuidarme, animarme, apoyarme y nunca dejar que diera un paso atrás frente a las oportunidades que fueron surgiendo en el camino, incluso cuando estas nos desafiaran personalmente.

Resumen

En entornos de baja metalicidad, la escasa abundancia de polvo reduce la capacidad de las nubes moleculares para protegerse de la radiación ultravioleta lejana, lo que favorece la fotodisociación del monóxido de carbono (CO) y da lugar a envolturas extendidas de gas molecular con débil o nula detección en CO ("CO-faint" o "CO-dark", respectivamente). En este contexto, la línea de emisión proveniente de la estructura fina de [C II], a 158 μm, constituye uno de los principales mecanismos de enfriamiento del medio interestelar y un trazador fundamental de estas fases moleculares poco visibles en CO.

El objetivo de este trabajo es caracterizar el origen multifásico de la emisión de [C II] y cuantificar la fracción de gas molecular que no es detectada en CO en distintas regiones de la Pequeña Nube de Magallanes. Esta galaxia, con una metalicidad de $\sim$0.2 $Z_\odot$, representa el laboratorio más cercano para estudiar las condiciones físicas propias de entornos de baja metalicidad, análogos a los de las galaxias en el universo temprano, y así poner a prueba modelos de regiones de fotodisociación.

Para ello, combinamos observaciones de alta resolución espectral de la línea [C II] a 158 μm, obtenidas con SOFIA/GREAT y upGREAT, junto con datos de CO(2–1) de APEX y el mapa de [H I] a 21 cm de ATCA+Parkes. A partir de estos datos realizamos una descomposición espectral de la emisión de [C II] en sus componentes atómica y molecular. Mediante un enfoque de descomposición lineal, estimamos las fracciones de [C II] asociadas a [H I] y H_2, y convertimos la componente molecular en densidades de columna asumiendo condiciones típicas de regiones de fotodisociación, restringidas por estudios previos de la Nube Pequeña de Magallanes. Posteriormente, comparamos el contenido de gas molecular obtenido con estimaciones basadas en CO y con la densidad superficial de la tasa de formación estelar local, $\Sigma_{\rm SFR}$,derivada a partir de los trazadores Hα y $L_{\rm TIR}$.

Encontramos que, el ancho de línea de [C II] en las líneas de visión analizadas se sitúa sistemáticamente entre los anchos de línea de [H I] y CO, lo que indica que su emisión se origina tanto del gas atómico como molecular. En promedio, $(81 \pm 1)\%$ de la intensidad de [C II] proviene de la fase molecular, mientras que $(15 \pm 1)\%$ está asociada al gas atómico. El H_2 trazado por [C II] representa aproximadamente $(77 \pm 4)\%$ de la densidad de columna total de gas molecular, lo que indica que

el reservorio molecular de la Nube Pequeña de Magallanes está dominado por gas "CO-dark". Además, no encontramos correlaciones significativas entre la fracción de gas "CO-dark" y la densidad de columna total, ni con ΣSFR, lo que sugiere que la abundancia de este componente está controlada principalmente por la eficiencia del blindaje por polvo y gas, más que por la actividad reciente de formación estelar.

En conjunto, estos resultados demuestran que [C II] es el principal trazador del gas molecular en la SMC y confirman la presencia de una fase molecular "CO-dark" extensa y estable en entornos de baja metalicidad. Esto tiene implicancias importantes para la interpretación de observaciones de [C II] en galaxias no resueltas, tanto en el universo local como a alto "redshift", donde el CO puede no representar completamente el contenido total de gas molecular.

Keywords – [C II] 158 μm, gas molecular, gas "CO-dark", Nube Pequeña de Magallanes, ISM, baja metalicidad, formación estelar

Abstract

In low-metallicity environments, the reduced dust abundance debilitates the shielding of molecular clouds against far-ultraviolet (FUV) radiation, enhancing CO photodissociation and producing extended envelopes of “CO-faint” or “CO-dark” molecular gas. The [C II] 158 μm fine-structure line is one of the brightest coolants of the interstellar medium (ISM) and a key tracer of these CO-faint molecular phases.

We aim to characterize the multiphase origin of the [C II] line emission and quantify the fraction of molecular gas that remains undetected in CO across several regions of the Small Magellanic Cloud (SMC), the nearest low-metallicity ($\sim$0.2 $Z_\odot$) galaxy that provides an ideal laboratory for testing photodissociation region (PDR) models under conditions that resemble those in early galaxies.

We combine high spectral resolution SOFIA/GREAT and upGREAT [C II] 158 μm observations with APEX CO(2–1) data and the ATCA+Parkes H I 21 cm map to perform a spectral decomposition of the [C II] emission into its atomic and molecular contribution. Using the linear decomposition approach, we derive the [C II] fractions associated with H I and H_2, and convert the molecular component into column densities assuming typical PDR conditions constrained by previous SMC studies. We then compare the resulting molecular gas content with CO-based estimates and with the local star formation rate surface density ($\Sigma_{\rm SFR}$) derived from Hα and $L_{\rm TIR}$ tracers.

The [C II] line width in the analyzed SMC lines of sight consistently falls between the H I and CO line widths, indicating that the [C II] emission arises from both molecular and atomic gas. On average, $(81 \pm 1)\%$ of the [C II] intensity originates from the molecular phase, while $(15 \pm 1)\%$ is associated with atomic gas. The [C II]-traced H_2 accounts for roughly $(77 \pm 4)\%$ of the total molecular gas column density, implying that the SMC’s molecular reservoir is dominated by CO-faint gas. This estimation yields to a calibrated H_2-to-CO conversion factor $X_{CO} \approx 7.94 \times 10^{20}$ cm^{-1}(K km s^{-1})$^{-1}$, 4 times larger than the canonical Galactic conversion factor. We find no significant correlation between the CO-dark fraction and either total column density or $\Sigma_{\rm SFR}$, suggesting that the abundance of CO-faint gas is primarily governed by the efficiency of dust and gas shielding rather than by current star formation activity.

Our results demonstrate that [C II] is the dominant tracer of molecular gas in the SMC and confirm the prevalence of an extended, stable CO-dark molecular phase in low-metallicity environments. This has important implications for interpreting [C II] observations in unresolved galaxies, both locally and at high redshift, where CO may not fully trace the molecular gas reservoir.

Keywords – [C II] 158 μm, molecular gas, CO-dark gas, Small Magellanic Cloud, ISM, low metallicity, star formation

List of Abreviations

α_{CO}	CO-to-H_2 conversion factor
Σ	surface density
A_ν	visual extinction
A_{ul}	spontaneous emission rate coefficient from the upper to lower level
ALMA	Atacama Large Millimeter/submillimeter Array
APEX	Atacama Pathfinder Experiment
ATCA	Australian Telescope Compact Array
C^+	ionized carbon
C^0	neutral carbon
CLASS	Continuum and Line Analysis Single-dish Software
CNM	cold neutral medium
CO	carbon monoxide
FUV	far-ultraviolet
FIR	far-infrared
FWHM	full width at half maximum
GREAT	German Receiver for Astronomy at Terahertz Frequencies
HERITAGE	*Herschel* Inventory of the Agents of Galaxy Evolution
H_2	molecular hydrogen
I	integrated intensity
IMF	initial mass function
ISM	interstellar medium
L	luminosity
LFA	Low Frequency Receiver
LMC	Large Magellanic Cloud
LOS	line of sight
$L_\odot$	Solar luminosity
LSRK	local standard of rest kinematic
LTE	local thermodynamic equilibrium
M_*	stellar mass
$M_\odot$	Solar mass
MW	Milky Way
$N(H_2)$	molecular hydrogen column density

n_{crit}	critical density
PAHs	polycyclic aromatic hydrocarbons
PACS	Photoconductor Array Camera and Spectrometer
PDR	photodissociation region
R_{ul}	collisional de-excitation rate coefficient from the upper to lower level
SED	spectral energy distribution
SFR	star formation rate
SMC	Small Magellanic Cloud
SNR	signal-to-noise ratio
SOFIA	Stratospheric Observatory for Infrared Astronomy
SPIRE	Spectral and Photometric Imaging Receiver
TIR	total Infrared
U	radiation field
upGREAT	upgraded German Receiver for Astronomy at Terahertz Frequencies
WNM	warm neutral medium
X_{CO}	CO-to-H_2 conversion factor
Z	metallicity
$Z_{\odot}$	Solar metallicity
[C I]	neutral carbon forbidden transition
[C II]	singly ionized carbon forbidden transition
[H I]	neutral atomic hydrogen
[N II]	singly ionized nitrogen forbidden transition
[O I]	neutral oxygen forbidden transition

Contents

List of Tables

List of Figures

Chapter 1

Introduction

Understanding how gas is transformed into stars is one of the main questions in astrophysics. Star formation plays a key role in galaxy formation and evolution, regulating the conversion of gas into stars and enriching the ISM through stellar feedback (Kennicutt and Evans (2012)). The rate at which gas is converted into stars correlates with the amount of molecular material, as expressed in the empirical Kennicutt–Schmidt relation, where the surface density of star formation scales with the gas surface density ($\Sigma_{\rm SFR} \propto \Sigma_{\rm gas}^{1+p}$; Kennicutt (1998); Kennicutt et al. (2009)). Due to this, tracing the molecular gas accurately is essential to understanding the physical mechanisms that control star formation efficiency in different galactic environments (Sun et al. (2018); Leroy et al. (2016)).

Observationally, the challenge of studying this cold gas phase lies in tracing the molecular components of the ISM, which is composed mainly of H_2. Molecular hydrogen is the most abundant molecule in the Universe, yet it is difficult to observe directly because it lacks a permanent dipole moment and its rotational transitions are not excited under typical cold ISM conditions (Bolatto et al. (2013)). For this reason, astronomers depend on indirect molecular gas tracers, such as low transitions of CO or the far-infrared fine-structure line of ionized carbon, [C II] 158μm, to infer the presence and amount of cold molecular gas (Crawford et al. (1985); Wolfire et al. (2010); Cormier et al. (2019)).

However, the reliability of these tracers strongly depends on the environmental conditions. In particular, in low-metallicity systems the reduced dust-to-gas ratio weakens the shielding of molecular clouds against far-ultraviolet radiation, enhancing the photodissociation of CO while leaving H_2 largely self-shielded. As a consequence, a significant fraction of the molecular gas reservoir becomes "CO-faint" or "CO-dark", remaining undetected in CO observations while still contributing substantially to the total H_2 mass (Wolfire et al. (2010); Bolatto et al. (2013)).

In this regime, the [C II] 158 μm line becomes a crucial tracer of molecular gas. The transition at 158μm originates from the $^2P^0_{3/2} \rightarrow^2 P^0_{1/2}$ level of ionized carbon (C^+), with an excitation energy of 91 K (Crawford et al. (1985)). Since carbon has a lower ionization potential (11.26 eV) than hydrogen (13.6 eV), C^+ can exist in a variety of environments, including the cold and warm neutral medium (CNM/WNM), the outer layers of molecular clouds (photodissociation regions), and weakly ionized gas. In PDR models, [C II] is expected to dominate the cooling in regions where CO is photodissociated but H_2 remains self-shielded (Kaufman et al. (1999, 2006); Wolfire et al. (2010); Hollenbach et al. (2012)). Observationally, the [C II] line is one of the brightest far-infrared (FIR) emission lines in galaxies and a major coolant of the ISM (Herrera-Camus et al. (2018); Cormier et al. (2019)).

Within the PDR framework developed by Kaufman et al. (1999, 2006), [C II] emission arises mainly from the surface layers of molecular clouds exposed to FUV radiation, where hydrogen transitions from the atomic to the molecular phase and carbon changes from C^+ to C and then to CO. The relative intensities of [C II], [C I], and CO therefore describe the structure of the gas across this transition. In dense PDRs, [C II] traces the warm molecular surface where H_2 is already formed but CO is photodissociated, while in diffuse gas it can originate from neutral atomic layers or low-ionization regions. Interpreting [C II] as a molecular tracer thus requires separating its various phase contributions, ideally by comparing velocity-resolved spectra of [C II], CO, and [H I], and by constraining possible ionized contributions through lines such as [N II] 205 μm (Herrera-Camus et al. (2016); Tarantino et al. (2021)).

At low metallicity, where both the dust-to-gas ratio and carbon abundance are reduced, PDR models predict an increase in the [C II]-emitting envelope relative to the CO core (e.g. Wolfire et al. (2010); Hollenbach et al. (2012)). This shift enhances the [C II]/CO luminosity ratio and implies that a large fraction of the molecular gas is CO-faint. Empirically, this behavior has been observed in nearby dwarf galaxies such as the LMC and SMC (Israel and Maloney (2011); Jameson et al. (2018); Okada et al. (2019)), as well as in other low-metallicity systems (Cormier et al. (2019); Madden et al. (2020)).

Recent studies in Galactic and extragalactic environments have shown that [C II] emission can trace a significant fraction of molecular gas not visible in CO (Pineda et al. (2014); Langer et al. (2014); Jameson et al. (2018); Tarantino et al. (2021)). However, because [C II] arises from multiple ISM phases, separating its molecular, atomic, and ionized contributions requires combining it with complementary tracers such as CO and [H I] at matched velocity resolution (Okada et al. (2015); Requena-Torres et al. (2016)). This is particularly important in low-metallicity environments, where complex and blended line profiles can obscure the underlying physical structure if only integrated quantities are considered.

The impact of these effects is particularly evident in nearby low-metallicity galaxies, where observations have revealed that a large fraction of the molecular gas is not traced by CO but instead by [C II] emission. This is reflected in enhanced [C II]/CO ratios and the presence of extended molecular envelopes surrounding compact CO cores (Madden et al. (2020); Okada et al. (2019); Jameson et al. (2018)).

The Small Magellanic Cloud (SMC) provides an ideal laboratory for studying these effects. Its proximity (∼61 kpc), stellar mass ($\log(M_*/M_\odot) = 8.5$), and metallicity of $\sim 0.2\ Z_\odot$ allow spatially resolved studies of the ISM while probing conditions similar to those in early galaxies. Previous works have revealed CO-faint molecular gas on large scales in the SMC (e.g. Sandstrom et al. (2010)), and velocity-resolved SOFIA/GREAT observations have shown that a large fraction (∼60%) of the molecular gas resides in extended CO-faint envelopes traced by [C II] emission (Requena-Torres et al. (2016)).

Jameson et al. (2018) further investigated the relationship between [C II]-bright and CO-bright gas using *Herschel* and ALMA spectroscopy of several SMC regions, including SWbarS, SWbarN, N22, N83, and SWDarkPeak, finding that on average ∼70% of the molecular gas is associated with [C II]-bright emission. By comparing integrated intensities and spatial distributions, they showed that [C II] preferentially traces extended molecular envelopes surrounding compact CO cores, consistent with PDR expectations at low metallicity.

Despite these advances, a detailed, velocity-resolved characterization of the multiphase origin of the [C II] emission and a quantitative census of the molecular gas reservoir traced by [C II] across different environments in the SMC remain essential. Disentangling the atomic and molecular contributions to the [C II] line is key to accurately constraining the total H_2 content and understanding the role of CO-dark gas in regulating star formation.

In this context, we combine new velocity-resolved SOFIA/GREAT [C II] 158 μm observations toward 10 lines of sight across the SMC with APEX CO and ATCA [H I] data to (i) determine the kinematic properties (centroid and linewidth) of [C II] relative to atomic and molecular gas, (ii) decompose the [C II] emission into its molecular and atomic components, (iii) estimate the H_2 column densities traced by [C II] and compare them with CO-based values, and (iv) relate these results to the SMC's dust and star-formation properties derived from infrared SED modeling. Together, these analyses provide a self-consistent picture of how [C II] emission traces the multiphase ISM in a low-metallicity environment and quantify the fraction of the molecular gas reservoir that remains undetected in CO.

1.1 The need of a CO-to-H_2 conversion factor

While CO is the most widely used tracer of molecular gas, converting its observed emission into a molecular hydrogen mass requires the adoption of a CO-to-H_2 conversion factor, commonly denoted as $X_{\rm CO}$ or $\alpha_{\rm CO}$. This factor relates the integrated CO intensity to the H_2 column density (or mass surface density) and is typically calibrated in the Milky Way using virial mass estimates, dust-based measurements, or γ-ray observations (Bolatto et al. (2013)).

In environments with near-solar metallicity, $X_{\rm CO}$ is found to be relatively constant, reflecting the fact that CO emission traces well-shielded molecular gas where the carbon is predominantly in molecular form. However, this assumption breaks down in low-metallicity systems, where reduced dust shielding allows far-ultraviolet radiation to penetrate deeper into molecular clouds. As a result, CO-emitting regions become confined to the densest and most shielded cores, while a significant fraction of the molecular gas resides in more extended envelopes where CO is photodissociated but H_2 survives (Wolfire et al. (2010); Bolatto et al. (2013)).

This effect leads to a systematic increase in the CO-to-H_2 conversion factor with decreasing metallicity, as CO traces only a subset of the total molecular gas reservoir. Observational studies of nearby dwarf galaxies, including the Magellanic Clouds, have shown that X_{CO} can be an order of magnitude or more higher than the canonical Galactic value (P. (1997); Leroy et al. (2011); Bolatto et al. (2013)). Consequently, relying solely on CO emission can lead to a significant underestimation of the total H_2 content in these environments.

These limitations highlight the importance of complementary tracers such as [C II] and dust emission to obtain a more complete census of the molecular gas. In particular, combining CO with tracers sensitive to CO-dark H_2 allows for a more accurate determination of the total molecular gas reservoir and provides critical constraints on the variation of X_{CO} across different physical conditions.

1.2 Outline of the thesis

Chapter 2 introduces the theoretical and observational concepts required to interpret the [C II] emission and molecular gas properties analyzed throughout this thesis. We first describe the physical structure of PDRs, focusing on the interaction between far-ultraviolet radiation and neutral gas, the thermal balance regulated by gas heating and cooling processes, and the layered transition between C^+, C^0, and CO inside molecular clouds.

And chapter 3 presents the observational dataset used throughout this thesis and describes the selection criteria applied to define the final sample analyzed. The chapter explains how the final set of analyzed regions was defined based on the availability of matched [C II], CO, and [H I] observations, signal-to-noise requirements, and kinematic consistency between the molecular and ionized carbon tracers.

Then chapter 4 describes the methodology adopted to characterize the physical conditions of the Small Magellanic Cloud interstellar medium and to quantify the molecular gas traced by [C II] and CO emission. The chapter combines infrared dust modeling, star formation diagnostics, spectral-line kinematic analysis, and emission-line decomposition techniques to construct a consistent framework for studying the multiphase structure of the low-metallicity ISM.

Finally, chapter 5 presents the main observational and physical results derived from the analysis of the [C II], CO(2–1), and [C I] emission in the selected SMC regions. The discussion is organized around four key aspects: (i) the kinematic comparison between the different gas tracers, (ii) the decomposition of the [C II] emission into molecular and atomic components, (iii) the molecular gas content traced by [C II] and CO, and (iv) the implications for the CO-to-H_2 conversion factor in low-metallicity environments. Special attention is given to the SWDarkPeak region, which provides a clear example of the transition between CO-bright and CO-dark molecular gas.

Chapter 2

Basic Concepts

2.1 PDR model

Photodissociation regions correspond to predominantly neutral interfaces between ionized and neutral molecular gas that are exposed to FUV photons in the energy range 6-13.6 eV. These photons regulate the thermal balance, chemistry, and structure of the gas without ionizing hydrogen. In PDRs, gas heating is mainly driven by the photoelectric effect on small dust grains and polycyclic aromatic hydrocarbons (PAHs), where FUV photons eject energetic electrons that transfer kinetic energy to the surrounding gas (Bakes and Tielens (1994); Hollenbach and Tielens (1999)). The dominant cooling channels depend on the local density and temperature, but are typically governed by far-infrared fine-structure lines such as [C II] 158 μm and [O I] 63/145 μm, together with low-J rotational transitions of CO deeper inside the cloud (Hollenbach and Tielens, 1999).

The classical PDR framework predicts a layered chemical structure controlled by the penetration of FUV radiation into the cloud (Tielens and Hollenbach (1985); Kaufman et al. (1999); Hollenbach and Tielens (1999)). In the left panel of Figure 2.1.1 is shown that at low visual extinctions ($A_V \lesssim 1$), carbon is predominantly ionized (C^+), producing strong [C II] emission from the warm surface layers. As the extinction increases and the FUV field becomes attenuated, carbon recombines into neutral atomic carbon (C^0), traced by the [CI] fine-structure lines. Deeper into the cloud ($A_V \gtrsim$ 2-4, depending on metallicity and density), CO becomes self-shielded and dominates the carbon reservoir, while the gas temperature decreases

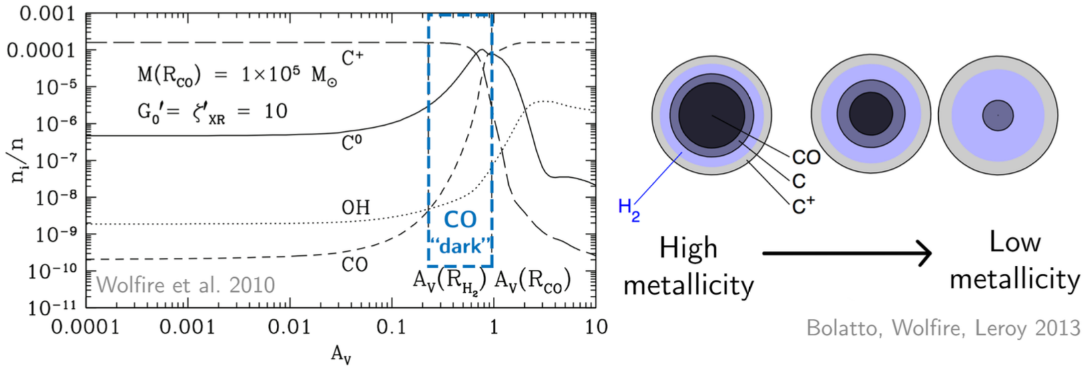

Figure 2.1.1: *(Left)* Abundances of C+, C and CO as functions of optical depth A_ν within a molecular cloud from Wolfire et al. (2010). The blue dashed box shows the range of AV values where the H2 gas is CO-faint (or CO-dark) and thus can be better traced by [C II] and [C I] emission. *(Right)* Effect of metallicity on CO and H_2 in a spherical clump immersed in a uniform radiation field from Bolatto et al. (2013). As the metallicity of the cloud decreases, the CO emitting region (dark grey) is pushed further into the clump.

and CO rotational transitions become the main cooling mechanism. Molecular hydrogen forms at shallower depths than CO because H_2 self-shields much more efficiently against photodissociation (Wolfire et al. (2010); Bolatto et al. (2013)). As a consequence, an intermediate layer of molecular gas can exist in which hydrogen is predominantly molecular while carbon remains in ionized form, giving rise to the so-called CO-dark molecular gas phase traced by [C II].

Increasing the FUV radiation field G_0 enhances gas heating and pushes the C^+/CO transition deeper into the cloud, while higher gas densities favor molecular formation and more efficient shielding. PDR models therefore predict specific line ratios such as [C II]/CO, [C II]/[C I] and [C I]/CO as a function of n_H and G_0, allowing observational constraints on the physical conditions of the molecular gas (Kaufman et al., 2006). In low-metallicity environments, the reduced dust-to-gas ratio weakens FUV attenuation and enlarges the C^+-emitting envelope relative to the CO core, substantially increasing the fraction of CO-dark molecular gas (Wolfire et al. (2010); Hollenbach et al. (2012); Madden et al. (2020)), as shown in the right panel of Figure 2.1.1.

2.1.1 CO-dark gas

CO-dark (or *CO-faint*) H_2 refers to molecular gas where H_2 survives by self-shielding but CO is photodissociated or underexcited, making it faint in CO while still present in other tracers. This component can be significant, especially in low-metallicity environments or under strong FUV radiation fields, and is often inferred from [C II], dust, or γ-ray constraints (Wolfire et al. (2010); Grenier et al. (2005); Langer et al. (2014)). In these environments, the reduced dust abundance weakens the attenuation of ultraviolet photons, allowing FUV radiation to penetrate deeper into molecular clouds and selectively destroy CO molecules while H_2 remains largely protected through self-shielding (Bolatto et al. (2013); Wolfire et al. (2010)). As a result, the molecular cloud structure develops extended C^+-emitting envelopes surrounding compact CO-bright cores, increasing the fraction of molecular gas that is invisible to standard CO observations. This effect is expected to become progressively more important at decreasing metallicity, where both the dust-to-gas ratio and the carbon abundance are reduced, leading to enhanced [C II]/CO ratios and larger reservoirs of CO-dark molecular gas (Madden et al. (2020); Cormier et al. (2019); Jameson et al. (2018)).

2.2 Surface density Star formation rate

The surface density of star formation quantifies the recent rate of stellar birth per unit area. Empirically, $\Sigma_{\rm SFR}$ correlates with gas surface density (the Kennicutt–Schmidt relation), with normalization and scatter influenced by local conditions and timescales Kennicutt (1998); Kennicutt and Evans (2012).

2.2.1 Unobscured SFR

Unobscured star formation is traced by the UV continuum and hydrogen recombination lines (e.g. Hα), which respond to massive, short lived stars over $\sim$ 5–100 Myr. These tracers require dust attenuation corrections and care with diffuse emission Kennicutt and Evans (2012); Hao et al. (2011).

2.2.2 Obscured SFR

Dust reprocessed emission in the infrared traces the obscured fraction of young stellar light. Total infrared (TIR) luminosity or selected monochromatic bands can be used alone or combined with Hα/UV in hybrid calibrations to recover total $\Sigma_{\rm SFR}$ Kennicutt et al. (2009); Calzetti et al. (2007); Kennicutt and Evans (2012).

2.3 Draine & Li 2007 dust model

The Draine et al. (2007) (DL07) considers that dust is exposed to a range of radiation fields U, within a range $U_{min} < U < U_{max}$, coming from a diffuse ISM component that is mostly dust. The DL07 model represents interstellar dust as a mixture of amorphous silicate and carbonaceous grains (with the smallest carbonaceous grains having the physical properties of PAH particles) heated by a distribution of starlight intensities parameterized by U_{min}, the least interstellar radiation field, and a power-law tail up to U_{max}, which represents the PDR component ($U > 100$). This dust emission model predicts full IR SEDs (3–1100 μm), enabling estimates of dust mass, PAH fraction, and radiation field parameters.

2.3.1 SMC infrared emission

Infrared emission from dust in the SMC has been observed by the Infrared Astronomical Satellite (IRAS; Schwering and Israel (1990); Sauvage et al. (1990)), the Diffuse Infrared Background Experiment (DIRBE) instrument on the Cosmic Background Explorer (COBE) satellite (Stanimirović et al., 2000). Li and Draine (2002) model the dust emission for the SMC Bar by assuming that the IR emission is due to the the carbonaceous grain population extends from grains with graphitic properties at radii $a \geq 0.01\mu$m down to particles with PAH-like properties at very small sizes. To constrain the model they use the observed 12, 25, 60, 100, 140, and 240 μm DIRBE band surface brightnesses $[\rm I]_{obs}$ and uncertainties from Stanimirović et al. (2000). The specified parameters are the column density of gas $N(H)$, the size distribution of the population that contributes to the PAHs and environmental properties, such as $\rm U_{min}$, $\rm U_{max}$ and β (dust emissivity spectral index, which characterizes the wavelength dependence of the grain opacity) (Li and Draine, 2002).

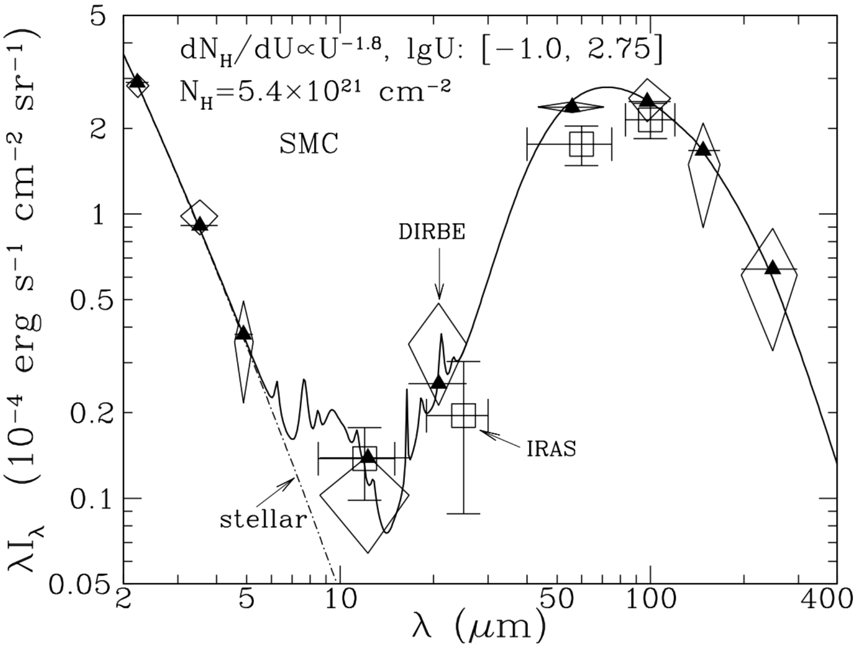

Figure 2.3.1: Comparison of the DL07 model (solid line) to the observed IR emission from the SMC by Li and Draine (2002). The measured emission obtained by COBE/DIRBE (diamonds) and IRAS (squares) is averaged over a 6.25 deg^2 region including the SMC optical bar and the Eastern Wing (Stanimirović et al., 2000). Triangles show the model spectrum convolved with the DIRBE filter.

In Figure 2.3.1 they show that their best-fit model reproduces the entire SMC spectrum with emission from dust ($N(H) \approx 5.4 \times 10^{21}$ cm^{-2}) illuminated by a wide range of starlight radiation with $U_{min} = 10^{-1.0}$, $U_{max} = 10^{2.5}$ and $\beta = 1.8$.

Chapter 3

Data and observations

3.1 Observations

We observed 17 line-of-sight (LOS) with SOFIA distributed in five SMC regions, namely N83, SWDarkPeak, SWbarN, N22, and SWbarS. These pointings are overlaid on the 160μm emission map of the SMC, as shown in Figure 3.1.1, and sample a diverse range of environments in terms of star formation activity, radiation field strength, and gas content. In this study, we make use of existing CO and [H I] observations.

3.1.1 SOFIA [C II] 158μm

Cycle 3 SOFIA [C II] ($^2P_{3/2}$–$^2P_{1/2}$) at 1900.5369 GHz (rest frame) observations ($\lambda \approx 157.7$ μm) were obtained for six regions in the SMC (Proposal ID 03_0120, PI Herrera-Camus; N22-R1, N22-R2, N22-R3, SWbarN-R4, SWbarN-R5, and SWbarN-R6) using the German Receiver for Astronomy at Terahertz Frequencies (GREAT). The [C II] line was detected with the L2 channel, which covers a radio-frequency range of 1815-1910 GHz. GREAT is a dual-channel heterodyne instrument for far-infrared (FIR) spectroscopy that provides high spectral resolution ($R \sim 10^8$) in several frequency windows in the 0.490–4.747 THz range, with a beam size of 14.1 (Heyminck et al. (2012)), which corresponds to ~ 4.3 pc for the SMC. The velocity resolution is $\Delta V \sim 0.1$ [km s^{-1}].

Cycle 5 SOFIA [C II] 158 μm observations targeting seven additional SMC regions (Proposal ID 05_0210, PI Herrera-Camus; N83-R1, N83-R2, N83-R3, N83-4,

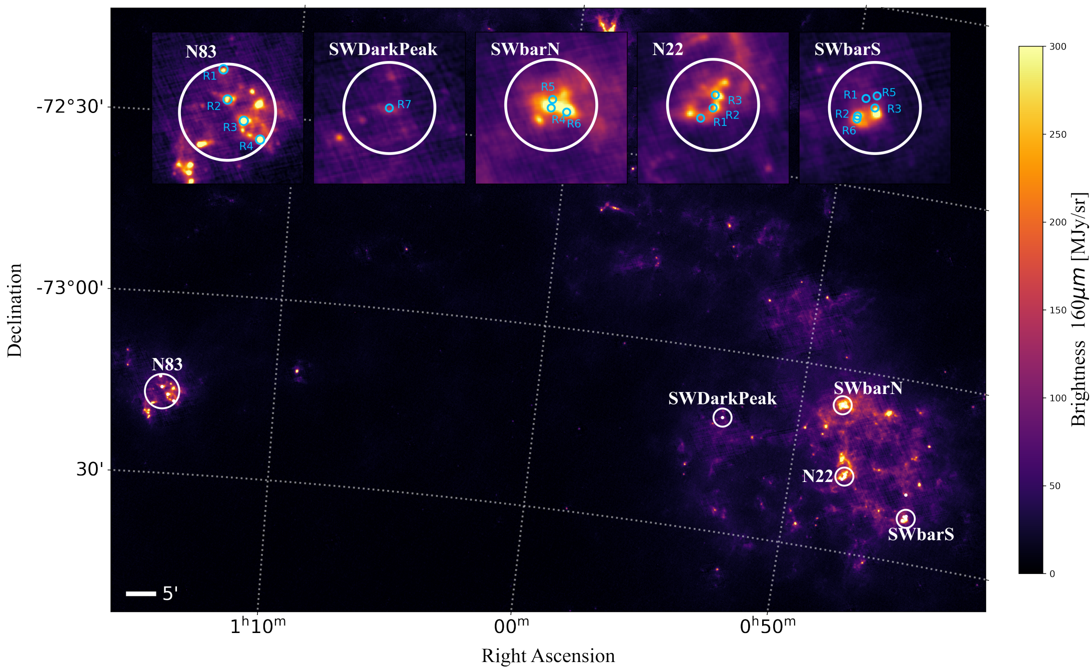

Figure 3.1.1: Far-infrared dust emission in the Small Magellanic Cloud (SMC). The background image shows the 160 μm surface brightness map obtained with the Herschel PACS instrument as part of the HERITAGE survey. White circles indicate the SMC regions analyzed in this study, and light blue circles mark the observed regions listed in Table 3.1.1

SWDarkPeak-R7, SWbarS-R5, and SWbarS-R6) were obtained with the upgraded GREAT (upGREAT) instrument, and a velocity resolution $\Delta V = 0.4$ [km s^{-1}]. The Low Frequency Array receiver (LFA) was used to detect the [C II] 158 μm transition over the frequency range 1459.6–1900.5 GHz. upGREAT is a multi-pixel, dual-polarization heterodyne receiver for FIR spectroscopy, providing high spectral resolution ($R \sim 10^8$) over multiple frequency bands in the 1.83–2.07 THz range for the LFA. The instrument's hexagonal array configuration provides seven beams per polarization, each with a FWHM beam size of ∼14.1 (Risacher et al. 2018) (∼ 4.3 pc).

The targets from Cycle 3 and Cycle 5 are shown in Figure 3.1.2, overlaid on the CO(2–1) integrated intensity maps. The selected SOFIA/GREAT pointings are distributed across the brightest CO structures in each region. In N22 and SWbarN (top panels), the observed positions trace the main molecular ridge and its associated star-forming clumps. In SWbarS and N83 (bottom left and right panels), the upGREAT array covers compact CO condensations as well as adjacent lower-intensity regions. The Hα contours reveal the location of ionized gas relative

Table 3.1.1: Observed SMC regions with the observed (*filled squares*) and unobserved (*open squares*) transitions and their coordinates (Eq.(J2000.0)), radial velocity, and different molecule/atom transitions that are available and studied in this work.

Region	RA	Dec	v_{LSR} [km s^{-1}]	HI	[C II]	^{12}CO(2-1)
N83-R1	1:14:24	-73:14:00	165	■	■	■
N83-R2	1:14:18	-73:15:45	165	■	■	■
N83-R3	1:14:04	-73:16:57	165	■	■	■
N83-R4	1:13:50	-73:18:00	165	■	■	■
SWDarkPeak-R7	0:52:53	-73:11:06	155	■	■	■
SWbarN-R4	0:48:27	-73:06:02	115	■	■	■
SWbarN-R5	0:48:20	-73:05:45	115	■	■	■
SWbarN-R6	0:48:18	-73:06:05	115	■	■	■
N22-R1	0:47:59	-73:18:01	120	■	■	■
N22-R2	0:47:54	-73:17:37	120	■	■	■
N22-R3	0:47:54	-73:17:11	120	■	■	■
SWbarS-R1	0:45:23	-73:22:22	120	■	□	■
SWbarS-R2	0:45:26	-73:22:59	120	■	□	■
SWbarS-R3	0:45:19	-73:22:40	120	■	□	■
SWbarS-R4	0:45:29	-73:18:45	120	■	□	■
SWbarS-R5	0:45:18	-73:22:13	130	■	■	■
SWbarS-R6	0:45:27	-73:23:05	130	■	■	■

to the molecular structures, showing that 9 of the [C II] pointings lie at the interface between bright CO emission and Hα peaks, consistent with photodissociation region (PDR) interfaces. In contrast, SWDarkPeak exhibits weaker and more diffuse CO emission, with the SOFIA positions sampling comparatively faint molecular gas.

3.1.2 APEX ^{12}CO(2-1)

The same regions observed in [C II] were also mapped in the rotational ^{12}CO$J = 2$–1 line using the 12m *Atacama Pathfinder Experiment* (APEX) telescope, located on the Llano de Chajnantor plateau in northern Chile (Güsten et al., 2006). The observations were performed with the Swedish Heterodyne Facility Instrument APEX-1, tuned to the rest frequency of 230.538 GHz for the ^{12}CO (2–1) transition. APEX-1 provides a half-power beam width of $\sim$27.5″ at this frequency (Vassilev et al., 2008).

The SMC CO(2–1) survey by Saldaño et al. (2023) includes the northeastern

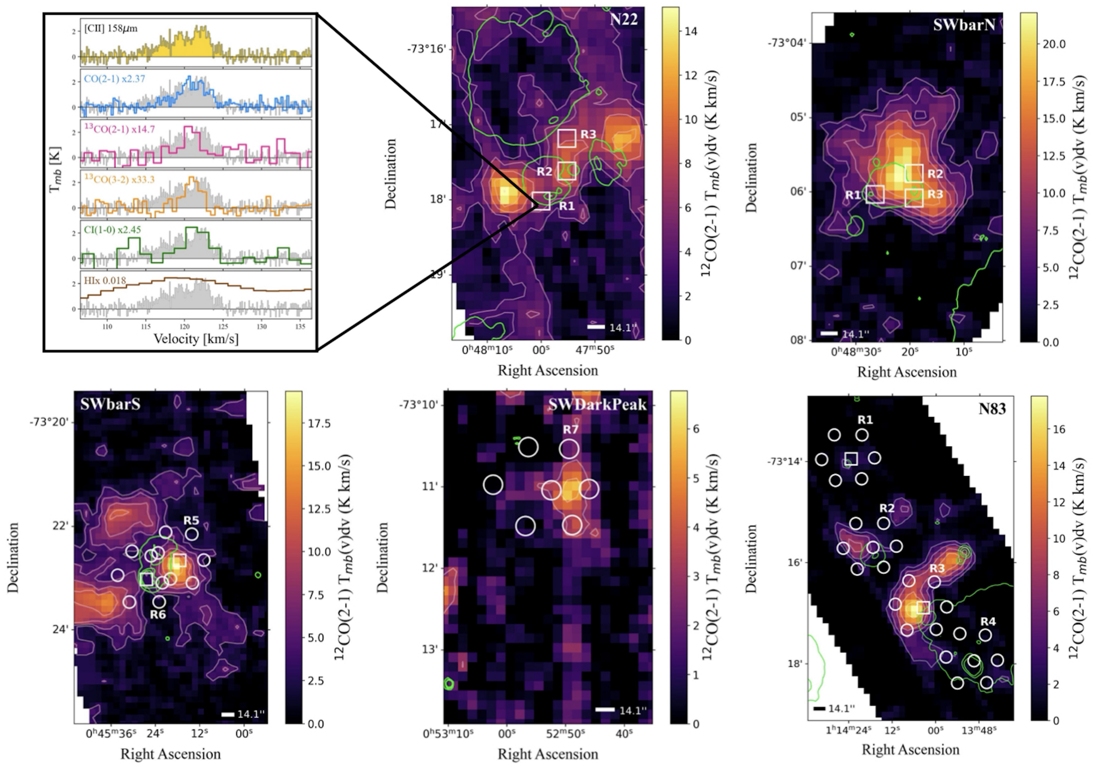

Figure 3.1.2: Spectral emission lines for the SMC region N22-R1 in [C II], [H I],[C I]and the different CO transitions on the left plot, normalized to the [C II] peak intensity, where it is shown that the [C II] 158 μm line profile lies between [H I] and the other low-J CO lines. Integrated intensity maps of APEX ^{12}CO(2-1) emission for the SMC regions *top right* N22 and SWbarN, *bottom* SWbarS, SWDarkPeak and N83. Light pink contours represent ^{12}CO(2-1) emission levels at 3σ, 5σ, 8σ, 11σ, and 15σ [K km s^{-1}], while lime green contours trace Hα emission at 3σ, 5σ, and 10σ significance levels erg cm^{-2} s^{-1}. The white circles indicate the locations of the 14.1SOFIA/GREAT (*top panels*) and the upGREAT 7-pixel array (*bottom panels*) 158μm observations for each SMC region (labeled as R$_i$, with $i = 1 - 7$). The white squares correspond to the regions selected for the analysis (See Section 3.3).

(N22), southwestern (SWBarN and SWDarkPeak), and Wing (N83) regions. The mapped fields of view were $24.8' \times 19.7'$, $20.9' \times 24.6'$, $5.5' \times 5.8'$, and $4.1' \times 13.8'$, respectively. The data cubes have typical rms noise levels between 0.1 and 0.7K, a spatial resolution of ∼9 pc, and a smoothed velocity resolution of $\Delta V = 0.25$ km s^{-1}.

3.2 Data

3.2.1 ATCA+Parkes [H I]

We make use of the neutral atomic hydrogen [H I] 21 cm data cube of the Small Magellanic Cloud obtained by combining observations from the Australia Telescope Compact Array (ATCA) and the Parkes 64 m single-dish telescope. The combined mosaic recovers both the large-scale diffuse emission measured by Parkes and the small-scale structure resolved by the ATCA interferometer (Stanimirović et al., 1999).

The observations cover an area of approximately $20° \times 18°$ centered on the SMC, with an angular resolution of 98" × 98" (corresponding to ∼20 pc at the distance of the SMC) and a spectral resolution of 1.65 km s^{-1} in the Local Standard of Rest kinematic (LSRK) frame. The [H I] data cube has an rms noise level of ∼1.3 K per channel (Stanimirović et al., 1999).

[H I] spectra were extracted at the positions of the SOFIA [C II] 158 μm pointings by sampling the 21 cm data cube at the corresponding sky coordinates.

3.3 Sample selection

We have 17 SOFIA pointings in total, of which 13 have simultaneous [C II] CO(2–1) and [H I] observations. Of these, 10 satisfy our signal-to-noise ratio (S/N) and velocity-shift criteria (Section 4.2) and are used in the decomposition analysis (Section 4.3); the remaining three: SWDarkPeak, N83-R2 and N83-R4, are discussed individually in Section 5.4 and 5.5.

Chapter 4

Methodology

4.1 Infrared luminosity and star formation rate of the SMC

Interpreting the [C II] emission in the SMC requires a careful characterization of both the dust-heated infrared output and the recent star formation activity. We therefore adopt infrared luminosities derived from full dust SED fitting and SFR estimates based on recombination-line emission, providing a consistent description of the physical conditions across the galaxy.

4.1.1 Infrared luminosity

The total infrared luminosity, $L_{\rm TIR}$, was measured using the SMC dust mixture maps from Chastenet et al. (2025), derived from the Draine and Li (2007) and Draine et al. (2007) models (hereafter DL07). For each region, the DL07 fit provides the mean starlight intensity $\langle U \rangle$ and dust mass $M_{\rm dust}$.

The 8–1000 μm TIR luminosity is given by:

$$L_{\rm TIR} = P_0 \langle U \rangle M_{\rm dust}, \quad \text{with} \quad P_0 = \frac{\text{power/H}}{\delta_{\rm d/H}, m_{\rm H}}, \qquad (4.1.1)$$

where $\delta_{\rm d/H} \equiv (M_{\rm dust}/M_{\rm H})_{\rm SMC} = 0.00206$ is the DL07 dust-to-hydrogen mass ratio for the SMC mixture, and $m_{\rm H}$ is the mass of a hydrogen atom. For the infrared power reradiated per H nucleon, P_0, we assume $U = 1$ and a fixed maximum radiation field $U_{\rm max} = 10^3$ for the power-law PDR component (e.g. Li and Draine, 002c; Aniano et al., 2012, 2020). The choice of the SMC DL07 mixture, characterized by a reduced PAH abundance and low dust-to-gas ratio, is appropriate for the SMC's low metallicity ($Z \approx 0.2\ Z_\odot$) and consistent with previous applications to the Magellanic Clouds (e.g., Draine and Li, 2007; Draine et al., 2007; Gordon et al., 2014).

4.1.1.1 Special case of region SWbarN

The DL07 dust parameter maps for the SMC contain some empty (NaN) pixels in the SWbarN region. Therefore, for SWbarN-R4, SWbarN-R5, and SWbarN-R6, we adopted an alternative approach to estimate $\Sigma_{\rm SFR}$. Instead of correcting the Hα luminosity with $L_{\rm TIR}$ derived from the DL07 mixture, we used the 160 μm emission map from the *Herschel* HERITAGE survey, which covers the SMC over $5° \times 5°$ (SPIRE) and $4° \times 3°$ (PACS) fields (Meixner et al., 2013), to obtain $L_{\rm TIR}$ and calculate the obscured star formation rate.

To calculate the TIR luminosity from the Herschel luminosity in the 160 μm band, we used the expression derived by Galametz et al. (2013):

$$log\, L_{TIR} = 1.024\, log\, \nu L_\nu(160\mu m) + 0.176, \tag{4.1.2}$$

with $a_{160} = 1.024$ and $b_{160} = 0.176$ the calibration coefficients, and $\nu L_\nu(160\mu m)$ the flux in the 160 μm band in $L_\odot$.

4.1.2 Star formation rate

We measure the star formation rate (SFR) of the SMC following the calibration by Kennicutt and Evans (2012):

$$\log {\rm SFR}\ [M_\odot\ {\rm yr}^{-1}] = \log L_{H\alpha} - \log C_{H\alpha}, \tag{4.1.3}$$

where the SFR calibration coefficient is $\log C_{H\alpha} = 41.26$ assuming a Kroupa (2001) IMF. The Hα line emission map for the SMC comes from the UM/CTIO Magellanic Cloud Emission-line Survey that covers the central $3.5° \times 4.5°$ of the

SMC at 3"–4" resolution with a photometric accuracy of ∼5% (Winkler et al., 2015).

To account for the obscured star formation traced by the dust continuum emission, we correct the Hα luminosity by combining it with the total infrared (TIR) luminosity, following Kennicutt et al. (2009):

$$L_{\mathrm{H}\alpha,\mathrm{corr}} = L_{\mathrm{H}\alpha,\mathrm{obs}} + 0.0024 L_{\mathrm{TIR}}. \tag{4.1.4}$$

The calibration coefficient adopted in Eq. 4.1.4 was derived from samples dominated by galaxies with higher metallicities than the SMC (Kennicutt et al., 2009). Consequently, the TIR contribution may underestimate the obscured star formation component in the SMC.

4.2 Line widths of [C II], CO and [H I]

A widely adopted approach to measure spectral line widths is to fit the observed line profiles with Gaussian functions, from which the full width at half maximum (FWHM) or the corresponding velocity dispersion can be derived (e.g., Muller E., 2010; Pineda et al., 2017). This method is well suited for lines that are approximately symmetric and dominated by a single kinematic component, and it provides a robust and homogeneous way to compare the dynamical properties of different gas tracers in the low-metallicity interstellar medium of the SMC (e.g., Rubio M., 2015).

Owing to the high velocity resolution of the available data (CO(2–1): $\sim 0.25\,\mathrm{km\,s^{-1}}$, [C II]: $\sim 0.1\,\mathrm{km\,s^{-1}}$, and [H I]: $\sim 1.65\,\mathrm{km\,s^{-1}}$), we are able to resolve narrow and complex features in the line profiles, particularly in the [C II] 158 μm emission. The top left panel of Figure 3.1.2 shows a comparison of the line profiles observed toward the N22-R1 region. The top panel presents the [C II] spectrum, which exhibits a complex velocity structure with asymmetric wings, indicating the presence of multiple kinematic components that cannot be adequately described by a single Gaussian function, as commonly found in low-metallicity star-forming regions (e.g., Herrera-Camus et al., 2015; Pineda et al., 2017). In contrast, the CO and ^{13}CO transitions display comparatively narrower and more symmetric profiles, tracing the denser molecular gas (e.g., Rubio M., 2015). The [H I] emission is significantly

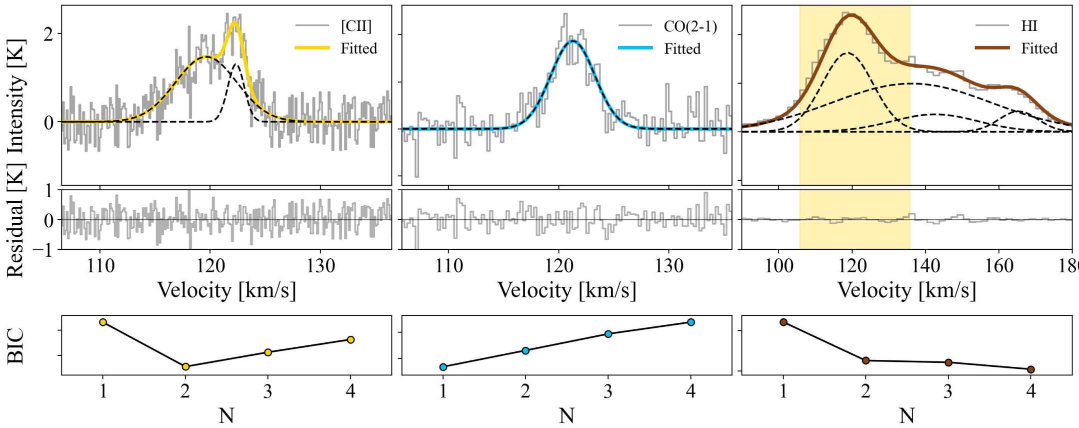

Figure 4.2.1: Multi-Gaussian fit to the [C II] 158μm (*left*), CO(2-1) (*middle*) and [H I] (*right*) emission lines (*gray*) from N22-R1. Individual Gaussian components are shown as black dashed lines. The middle panels show the fit residual for each tracer. The bottom panel plots illustrate the Bayesian Information Criterion as a function of the number of Gaussian components, N. For the [H I] spectrum we consider a broader velocity interval between 80 and 200 km s^{-1}, within which the BIC analysis reveals four distinct kinematic components. Among these, the component centered at ∼125 km s^{-1} coincides with the velocity range of the [C II] and CO emission shown in the spectra (*yellow shaded area*).

broader reflecting the widespread character and large velocity dispersion of the atomic gas, particularly its warm component (e.g., Stanimirović et al., 2004). These differences highlight the distinct kinematic regimes probed by each tracer and motivate a careful and homogeneous treatment of the linewidth measurements across gas phases.

To identify possible asymmetries, we perform multi-Gaussian fits and apply the Bayesian information criterion (BIC) to assess whether additional components significantly improve the fit. This approach allows us to identify spectra with deviations from a single Gaussian profile, while still adopting a FWHM as a uniform metric across the dataset. Figure 4.2.1 shows an example of this procedure for the region N22-R1. The middle panels present the resulting fits for the [C II] (gold), CO(2–1) (light blue), and [H I] (brown) native spectra (gray), together with the individual Gaussian components (black dashed lines). The middle panels show the corresponding residuals, meanwhile the bottom panels display the BIC as a function of the number of Gaussian components, where the minimum value indicates the preferred model complexity.

In this example, the BIC favors a multi-component description for the [C II] profile, while the CO(2–1) spectrum is well reproduced by a single Gaussian component. The [H I] line, in contrast, exhibits a broader and more structured profile requiring multiple components. N22-R1 therefore illustrates a behavior commonly observed across the SMC regions, where the [C II] 158 μm emission line displays a more complex kinematic structure than the CO(2–1) emission.

To determine which component of the multi-Gaussian [C II] fit should be compared with the CO and [H I] components, we define a velocity matching criterion based on the relative peak positions. Specifically, we adopt a tolerance range for the velocity offset between the [C II] peak and the CO and [H I] peaks of $\Delta v \sim 3$ km s^{-1}, corresponding to approximately 50% of the average single-component linewidth. This threshold allows velocity differences comparable to the channel width of the [H I] spectrum while remaining sufficiently restrictive to avoid associating clearly distinct kinematic components.

4.3 [C II] emission decomposition

To isolate the CO-faint molecular gas traced by the [C II] line emission, we first need to remove the contributions arising from the ionized and atomic gas phases. In low-metallicity star-forming regions, the [C II] emission associated with ionized gas is generally small compared to that originating in photodissociation regions (PDRs; Kaufman et al. 1999). Previous estimates of the ionized gas contribution to the total [C II] emission are typically $\leq 19\%$ in the LMC (e.g., Lebouteiller et al., 2012; Okada et al., 2015; Pineda et al., 2017) and $\leq 5\%$ in the SMC (e.g., Pineda et al., 2017; Requena-Torres et al., 2016). Jameson et al. (2018) presents Herschel PACS and SPIRE observations of these same regions in [C II] and [N II] emission and discusses the ionized gas contribution to [C II], concluding that it is at most 5%. For these reasons we neglect the contribution of ionized gas to the [C II] line emission of the SMC in this work.

To remove the atomic gas contribution to the [C II] emission, we apply the method introduced by Tarantino et al. (2021) for nearby galaxies, in which the [C II] line profile is modeled as a linear combination of the CO and [H I] line profiles, representing the molecular and atomic contributions, respectively. For the decomposition, we use Rayleigh–Jeans brightness temperatures as a measure of flux for the [C II], CO(J=2–1), and [H I] spectra:

$$T_{[\mathrm{CII}],\mathrm{model}} = w_{\mathrm{CO}} T_{\mathrm{CO}} + w_{\mathrm{HI}} T_{\mathrm{HI}}, \tag{4.3.1}$$

where w_{CO} and w_{HI} are the linear coefficients that best reproduce the observed [C II] emission, and $T_{[\mathrm{CII}],\mathrm{model}}$ is the modeled [C II] profile.

The coefficients are obtained through χ^2 minimization:

$$\chi^2 = \sum_{n=1}^{N} \frac{\left(T_{[\mathrm{CII}]} - w_{\mathrm{CO}} T_{\mathrm{CO}} - w_{\mathrm{HI}} T_{\mathrm{HI}}\right)^2}{\sigma^2_{[\mathrm{CII}]} + w^2_{\mathrm{CO}} \sigma^2_{\mathrm{CO}} + w^2_{\mathrm{HI}} \sigma^2_{\mathrm{HI}}}, \tag{4.3.2}$$

where σ represents the rms noise of each spectrum, and the model is evaluated across N spectral channels.

Once the linear coefficients are obtained, we calculate the fractions of [C II] emission associated with the molecular (f_{mol}) and atomic (f_{atomic}) phases:

$$f_{\mathrm{mol}} = \frac{w_{\mathrm{CO}} \int T_{\mathrm{CO}} dv}{\int T_{[\mathrm{CII}]} dv}, \qquad f_{\mathrm{atomic}} = \frac{w_{\mathrm{HI}} \int T_{\mathrm{HI}} dv}{\int T_{[\mathrm{CII}]} dv}. \tag{4.3.3}$$

Since the spectral lines were observed with different instruments, we rebinned the line profiles to a common velocity resolution $\Delta V \approx 1.65$ km s^{-1} to perform the analysis described above. For each [H I] velocity channel, we compute the mean [C II] and CO emission over the corresponding velocity range. This approach enables a direct, channel-by-channel comparison for estimating the linear coefficients. Regarding the spatial resolution, [H I] resolution is significantly poorer than that of the [C II] and CO (about a factor of $\sim$8). We decided not to convolve the [C II] and CO maps to the [H I] spatial resolution in order to preserve the level of detail of the analysis. We do not expect this to significantly impact the results, as the [H I] spatial distribution is expected to be smoother than that of [C II] and [C I] (See Figure 4.2.1).

An example is shown in Figure 4.3.1, where the solid lines represent the rebinned [C II] (gold), CO (light blue) and [H I] (brown), meanwhile the dashed black line corresponds to the modeled [C II] emission. The [C II] line profile lies between the [H I] and CO profiles, a behavior present in 9 out of the 10 analyzed regions. In addition, excess [C II] 158 μm emission at velocities that cannot be associated with CO is present in 8/10 of the regions (See Apendix A2).

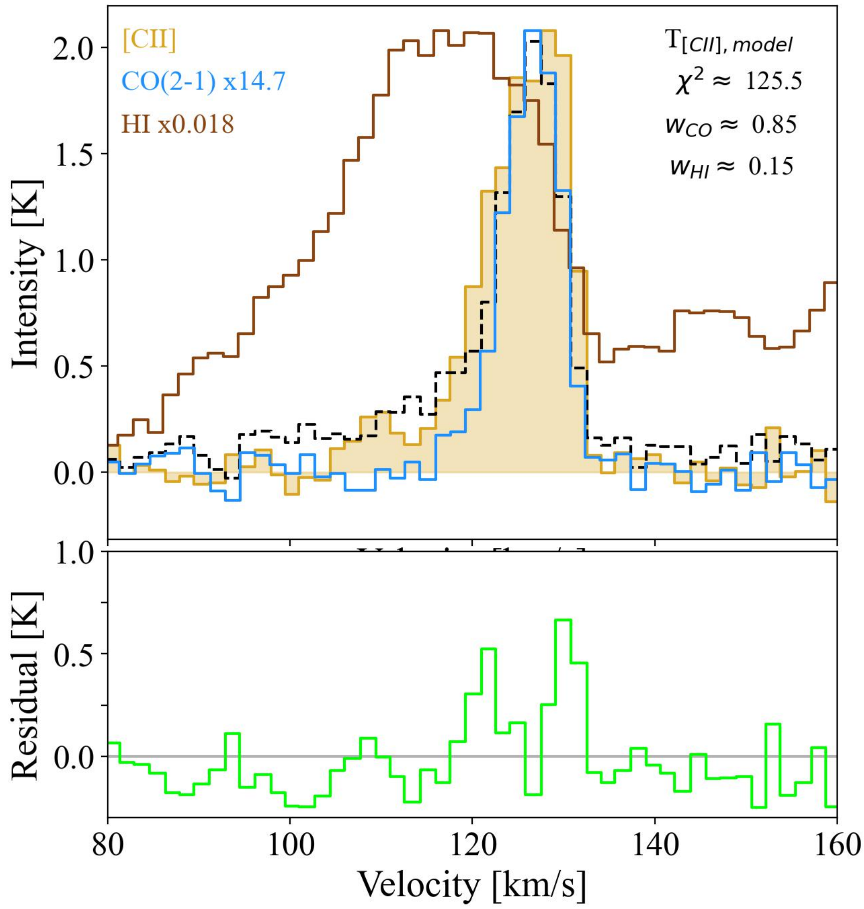

Figure 4.3.1: Rebined espectra of [C II] 158 μm *(yellow)*, CO(2-1) *(light blue)*, for SWbarS-R5, that match the [H I] line profile *(brown)* velocity resolution. The [H I] and CO spectra are normalized to the maximum intensity of the [C II] spectra. The dashed black line corresponds to the decomposed [C II] 158 μm emission with linear coefficients $w_{CO} \approx 0.85$ and $w_{HI} \approx 0.15$ and reduced $\chi^2_\nu \approx 1.63$ ($\chi^2 \approx 125.5$), estimated with the methodology described in Section 4.3.

4.4 Tracing H_2 with CO and [C II]

Due to the photodissociation of CO in the outer layers of an H II/PDR/molecular cloud complex, it is necessary to consider the contributions of both CO and [C II] emission to the total estimate of the H_2 column density:

$$N(H_2)_{\text{total}} = N(H_2)_{[\text{C ii}]} + N(H_2)_{\text{CO}}, \tag{4.4.1}$$

where $N(H_2)_{[\text{CII}]}$ and $N(H_2)_{\text{CO}}$ represent the molecular gas at low and high extinction, respectively. In this section, we derive $N(H_2)$ independently from [C II] and CO and quantify the fraction of molecular gas that is not traced by CO line emission in the low-metallicity environment of the SMC.

4.4.1 Converting $I_{[CII]}$ to $N(H_2)$

Studies of the [C II] 158 μm fine-structure emission from star-forming regions as a function of metallicity show that the [C II]-emitting gas envelope is optically thin for gas temperatures above 11 K (LMC: Israel F. P. (1996); SMC: Israel and Maloney (2011)). In this regime, the integrated line intensity due to collisional excitation can be expressed, in units of W m^{-2} sr^{-1}, as:

$$I_{[CII]} = 2.3 \times 10^{-24} \left(\frac{2e^{-91.2/T}}{1 + 2e^{-91.2/T} + n_{\rm crit}/n} \right) N_{[CII]}, \tag{4.4.2}$$

where n is the number density of the collisional partner (cm^{-3}), T is the gas temperature (K), and $n_{\rm crit}$ is the critical density, that is, the density at which the collisional de-excitation rate equals the spontaneous emission rate. The constant factor depends on the transition energy, the ratio of statistical weights, and the abundance of [C II] relative to hydrogen (Crawford et al., 1985).

The integrated intensity associated with the molecular gas phase for each spectrum is then given by

$$I_{[CII],\rm mol} = f_{\rm mol} \int T_{[CII]} dv, \tag{4.4.3}$$

where $I_{[CII],\rm mol}$ is in K km s^{-1} and dv is the velocity range of the rebinned [C II] emission. By converting the units in Eq. 4.4.3 and combining with Eq. 4.4.2, we obtain the H_2 column density:

$$N(H_2)_{[CII]} = \frac{4.35 \times 10^{23}}{(C/H)_{\rm SMC}} \left(\frac{1 + 2e^{-91.2/T} + n_{\rm crit}(H_2)/n}{2e^{-91.2/T}} \right) I_{[CII],\rm mol}, \tag{4.4.4}$$

where $(C/H)_{\rm SMC} = 2.8 \times 10^{-5}$ is the carbon abundance, derived by applying the SMC metallicity factor to the Milky Way value (Jameson et al., 2018).

The critical density for collisions with H_2 is

$$n_{crit}(H_2) = \frac{A_{ul}}{R_{ul}} \tag{4.4.5}$$

where the collisional de-excitation rate coefficient for [C II]–H_2 interactions, including hydrogen spin effects in LTE, is $R_{ul} = (4.55 + 1.6e^{-100/T}) \times 10^{-10}$ cm^3 s^{-1}

(Wiesenfeld and Goldsmith, 2014), and $A_{ul} = 2.1 \times 10^{-6}$ s^{-1} (Carilli and Walter, 2013). As an example, the critical density at T=$E_{ul}/k \approx 91.2$ K is therefore $n_{crit} \approx 4500$ cm^{-3}.

To convert the [C II] emission into a molecular gas column density, we first use Eq. 4.4.4 to calculate $N(H_2)_{[C II]}$ for each SMC region from the corresponding integrated molecular [C II] intensity, ($I_{[C II],mol}$), obtained from the decomposition analysis. The resulting column densities are then averaged to derive a mean value for the SMC. This conversion requires adopting representative gas conditions (density and temperature), which determine the [C II] excitation. We assume an average density (n = 4000) cm^{-3} and a temperature $T = 90$ K, following Jameson et al. (2018), consistent with warm and moderately dense PDRs. These values are based on the PDR models of Kaufman et al. (2006), with updated gas and grain-surface chemistry from Wolfire et al. (2010) and Hollenbach et al. (2012). At this temperature and density, the inferred H_2 column densities are approximately a factor of three larger than those obtained under the high-density, high-temperature limit corresponding to maximum [C II] excitation (Jameson et al., 2018).

4.4.2 Converting I_{CO} to $N(H_2)$

In the inner parts of molecular clouds, where shielding from the incident FUV radiation is sufficient to prevent CO from being photodissociated (Wolfire et al., 2010; Lee et al., 2015), the molecular gas column density can be estimated using the CO integrated intensity method,

$$N(H_2) = X_{CO} I_{CO}, \tag{4.4.6}$$

where $N(H_2)$ is the H_2 column density, X_{CO} is the CO-to-H_2 conversion factor in units of cm^{-2} (K km s^{-1})$^{-1}$, and I_{CO} is the rebinned CO integrated intensity in K km s^{-1}.

Although the low metallicity of the SMC is expected to increase the effective CO-to-H2 conversion factor, X_{CO}, owing to the presence of extended CO-faint molecular envelopes (e.g., Leroy et al., 2011), simulations by Shetty et al. (2011) have shown that, in the densest and CO-bright regions of molecular clouds in the SMC, the Galactic conversion factor estimated by Bolatto et al. (2008), $X_{CO,MW} \approx 2 \times 10^{20}$ cm^{-2} (K km s^{-1})$^{-1}$, which is the canonical value for CO(1-0) assuming a CO line ratio $R_{21} = 1$, can still provide a reasonable approximation. Furthermore, Jameson et al. (2018) estimated the conversion factor for CO-bright regions in the SMC and obtained median values of $X_{\mathrm{CO}} = (1.3\text{-}2.3) \times 10^{20}$ cm^{-2} (K km s^{-1})$^{-1}$, consistent with a Milky Way value of $X_{\mathrm{CO,MW}}$. Given these simulation results, we adopt a Galactic CO-to-H2 conversion factor of $X_{\mathrm{CO,MW}} = 2 \times 10^{20}$ cm^{-2} (K km s^{-1})$^{-1}$ (Bolatto et al., 2013) to estimate the molecular gas content in regions of high extinction where most of the carbon is in the form of CO. This choice is consistent with a scenario in which the main driver of the enhanced effective conversion factor in low-metallicity systems is the shrinking of the high-A_V CO-emitting cores and the growth of an outer H_2 layer coextensive with C^+ (e.g., Wolfire et al., 2010; Bolatto et al., 2013).

Chapter 5

Results and Discussion

5.1 Comparing velocities and line widths across tracers

We analyze the [C II] CO J=2-1, and HI spectra for 13 targets across five SMC regions (N83, SWDarkPeak, SWbarN, N22, SWbarS), using the common velocity rebinning described in Sect. 4.3 and the linear decomposition of [C II] into atomic and molecular components (Eqs. 4.3.1–4.3.3). This matched spectral resolution enables a tracer by tracer comparison of emission line profiles and integrated intensities, while our BIC tested multi-Gaussian fitted spectra give insights into the multiphase nature of the [C II] gas (Section 4.2).

The results of the velocity and line width comparison are presented in Figure 5.1.1, where the gray shaded region indicates the adopted velocity-shift tolerance relative to the [C II] centroid. We find that the [C II] line widths systematically lie between those of CO(2–1) and [H I], with CO typically exhibiting narrower profiles and [H I] broader ones. This trend supports a scenario in which [C II] traces a combination of gas phases, arising from both the dense molecular component associated with CO emission and a more diffuse or extended component linked to atomic gas (Okada et al. 2015; Requena-Torres et al. 2016; Okada et al. 2019). The distribution of points in the FWHM comparison further reinforces this interpretation. Most CO measurements lie close to or below ΔFWHM $= 0$, indicating that CO traces the kinematically colder and more confined molecular cores. In contrast, [H I] exhibits systematically larger line widths, consistent with a more turbulent and spatially

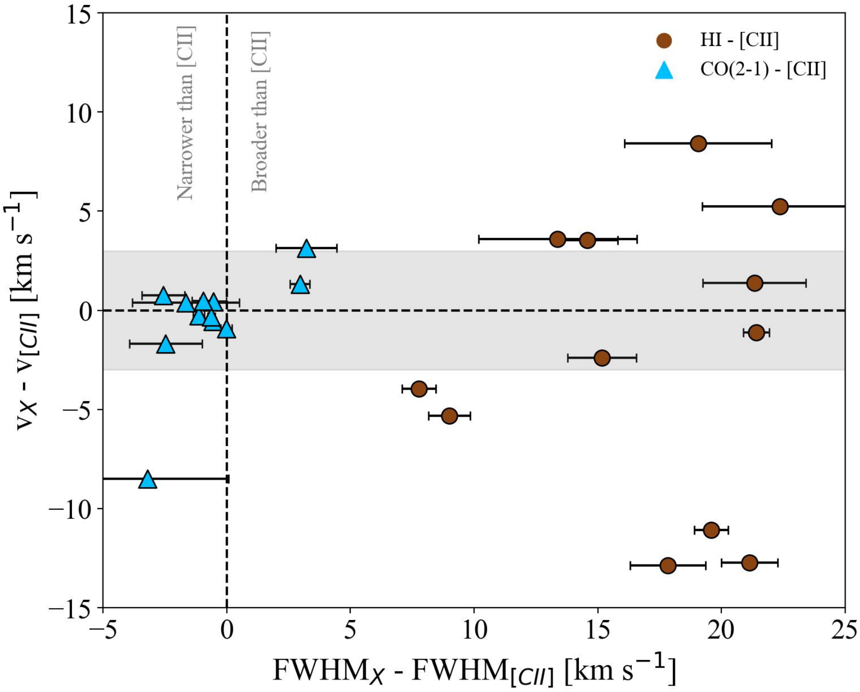

Figure 5.1.1: Line width comparison among the [C II] 158 μm, CO(2–1) (*circles*), and H I (*triangles*) emission line profiles. Points lying on the left side of x-axis correspond to regions where the tracers' line width is narrower than [C II]. Meanwhile, points on the right side, indicate regions where the CO and [H I] are broader than [C II]. The gray shaded area represents the velocity-shift tolerance range described in Section 4.2.

extended medium. The intermediate position of [C II] suggests that a significant fraction of its emission originates in molecular gas not traced by CO, commonly referred to as CO-dark H_2 (Wolfire et al. 2010; Pineda et al. 2013; Bolatto et al. 2013).

5.2 Decomposition analysis of the [C II] transition

The [C II] decomposition indicates that the gas associated with the CO-emitting molecular phase contributes, on average, $(81 \pm 1)\%$ of the total [C II] emission, dominating over the atomic contribution. This result is illustrated in Figure 5.2.1, which also compares our measurements with those of Jameson et al. (2018) for the SMC and Tarantino et al. (2021) for two nearby galaxies. Our results are in very good agreement with the SMC measurements of Jameson et al. (2018). In contrast, Tarantino et al. (2021) find a more balanced molecular and atomic

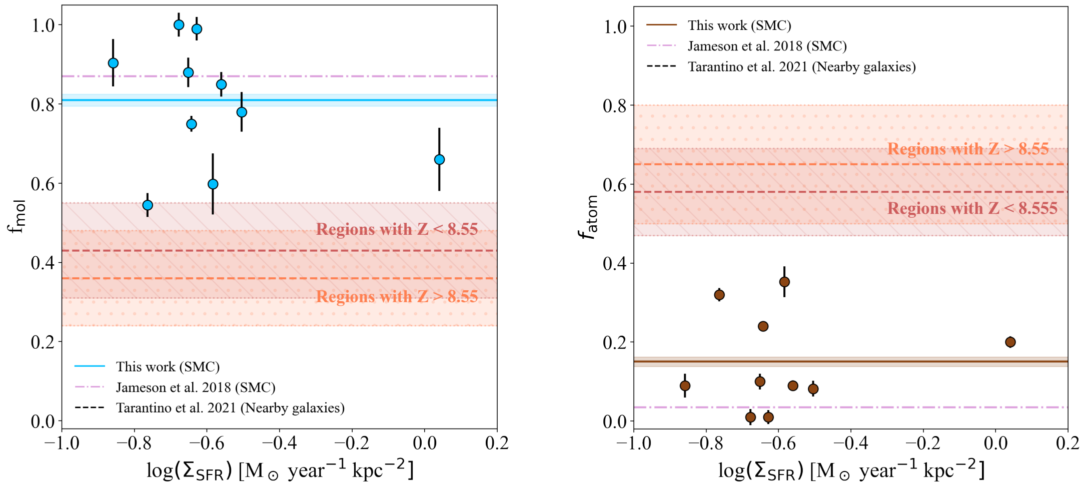

(a) **(b)**

Figure 5.2.1: Estimated [C II] 158 μm emission fractions associated with *(a)* CO-bright H_2 molecular gas and *(b)* [H I] atomic gas, based on the [C II] linear decomposition. The average [C II] fractions along the SMC targeted regions are indicated by the light blue and brown solid lines, where the shaded areas represent the average weighted error of the estimations. Both panels include the estimations of the [C II] 158 μm emission fractions made by Tarantino et al. (2021) for nearby galaxies (*clay and orange dashed lines*), with their corresponding error bands, and by Jameson et al. (2018) for the SMC (*pink dash-dotted line*), associated with the different gas phases.

contribution to the [C II] emission. We attribute this difference primarily to velocity and spatial resolution, and the metallicity of the studied regions. The analysis by Tarantino et al. (2021) has $\Delta V > 5$ [km s^{-1}] on $\sim$ 500 pc scales in M101 and NGC6946, while our work is on scales of $\sim$ 4 pc and a velocity resolution $\Delta V = 0.5$ [km s^{-1}]. Also, their regions are in environments with higher metallicities ($12 + log[O/H] = 8.31$–8.62 versus $12 + log[O/H]_{SMC} \sim 8.0$ for the SMC). These environmental conditions likely lead to a more evenly distributed molecular and atomic contribution to the [C II] 158 μm emission.

This result provides evidence for CO-faint H_2 gas traced by [C II] 158 μm emission in low-metallicity environments (Requena-Torres et al., 2016; Langer et al., 2014; Pineda et al., 2014, 2017). In most regions, the residual between the modeled [C II] emission profiles, based on the linear decomposition, and the observed spectra lies above the spectral noise level (see the bottom panel of Fig. 4.3.1). Furthermore, the positive residuals are generally concentrated near the velocity range where CO emission peaks (See Apendix A2), suggesting that this excess [C II] emission is kinematically associated with the molecular component rather than with unrelated atomic gas. This behavior is consistent with a scenario in which [C II] traces molecular gas that shares the same dynamical structure as the CO-emitting material but remains weak or undetected in CO due to photodissociation effects in low-metallicity environments, where reduced dust shielding allows UV photons to penetrate deeper into molecular clouds, enlarging the C^+/H_2 layer surrounding dense CO cores (Wolfire et al., 2010; Langer et al., 2014; Pineda et al., 2017). Therefore, the residual emission provides additional evidence for an extended reservoir of CO-faint molecular gas surrounding the denser CO-bright regions.

Regarding the rebinning to a common spectral resolution between [C II], CO, and [H I] we do not expect this to introduce systematic effects unless the components were extraordinarily narrow, which we do not observe in the lines at native spectral resolution.

Furthermore, no significant correlation is found between the molecular and atomic gas fractions associated with the [C II] emission on star formation rate surface density, $\Sigma_{\rm SFR}$, as shown in Figure 5.2.1. This lack of correlation suggests that the fraction of CO-faint gas is not mainly set by active in star formation a region is, but instead by how efficiently the gas and dust can shield molecules from the surrounding radiation field. Similar trends have been reported in other nearby dwarf galaxies (e.g. Lebouteiller et al. (2012); Madden et al. (2020)), where [C II] remains the main coolant of both quiet and active regions. These results indicate that in the SMC, the CO-dark molecular phase is extended and relatively stable, and its presence does not depend strongly on the current level of star formation.

5.3 The CO-faint gas in the SMC: Comparing the [C II]- and CO-based $N(H_2)$

In Figure 5.3.1 we show that the molecular hydrogen traced by [C II], $N(H_2)_{[C\,II]}$, accounts on average for roughly 77% of the total molecular gas column density, $N(H_2)_{\rm total}$. The column density values derived from CO, [C II], and their combined contribution (CO+[C II]) for each region are reported in Table 5.3.1. This corroborates that a substantial fraction of the molecular reservoir of the SMC is in the CO-faint phase, confirming results reported for the SMC using the same technique with Herschel PACS measurements (Jameson et al., 2018), as well other results using velocity-resolved [C II] data for low-metallicity systems (e.g., Pineda et al., 2014, 2017). The dominance of [C II]–bright, CO-faint gas emphasizes that the H_2 content inferred from CO alone would underestimate the true molecular mass by almost a factor of ∼4 under low-metallicity conditions.

Table 5.3.1: Average H_2 molecular gas column density estimates, based on CO, [C II] and CO+[C II], respectively, for the SMC regions.

SMC region	$\overline{N}(H_2)_{CO}$ [10^{21}cm^{-2}]	$\overline{N}(H_2)_{[CII]}$ [10^{21}cm^{-2}]	$\overline{N}(H_2)_{total}$ [10^{21}cm^{-2}]
N22	1.58 ±0.09	6.89 ±0.04	8.47 ±0.09
SWbarN	3.42 ±0.12	11.6 ±0.07	15.0 ±0.12
N83	2.23 ±0.06	5.52 ±0.02	7.75 ±0.07
SWbarS	1.90 ±0.15	6.52 ±0.04	8.42 ±0.15

Figure 5.3.1 also shows, however, that no significant correlation is found between $N(H_2)_{[C\,II]}/N(H_2)_{total}$ and either the total molecular column density or the star formation rate surface density, Σ_{SFR}. This lack of correlation suggests that the fraction of CO-faint gas is not mainly set by how dense or active in star formation a region is, but instead by how efficiently the gas and dust can shield molecules from the surrounding radiation field. Similar trends have been reported in other nearby dwarf galaxies (e.g. Lebouteiller et al. (2012); Madden et al. (2020)), where [C II] remains the main coolant of both quiet and active regions. These results indicate that in the SMC, the CO-dark molecular phase is widespread and relatively stable, and its presence does not depend strongly on the current level of star formation.

The aforementioned is consistent with the physical picture proposed for low-metallicity dwarf galaxies by Cormier et al. (2019), in which the reduced dust abundance produces a highly porous multiphase ISM, allowing far-ultraviolet radiation to penetrate deeper into molecular clouds. Under these conditions, the C^+/H_2 envelopes surrounding molecular clouds become spatially extended while the well-shielded CO cores shrink, increasing the fraction of molecular gas that remains invisible in CO emission.

We can use these data to compute a X_{CO} factor applicable on ∼ 4 pc scales near CO-bright regions of the SMC. By solving the equation 4.4.6 for X_{CO}, using $N(H_2)$ as the total molecular gas column density, and I_{CO} as the weighted average of the integrated CO(2-1) intensity across the SMC regions, we estimate a CO(2-1)

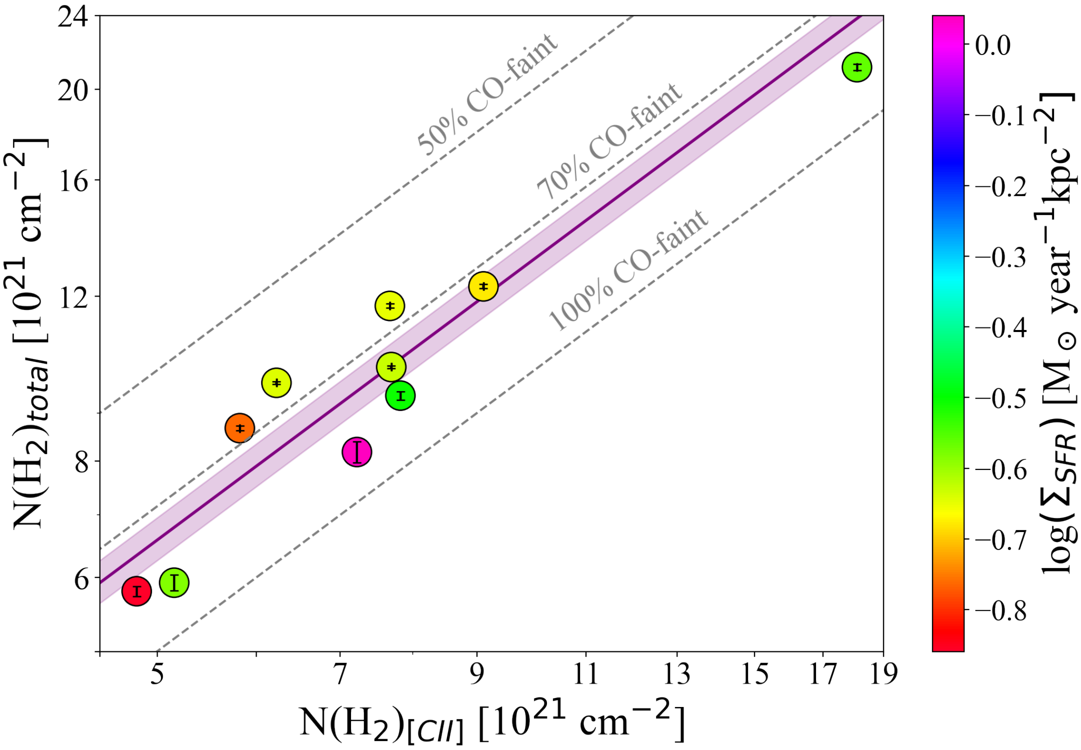

Figure 5.3.1: Total molecular hydrogen column densit,y $N(H_2)_{\text{total}}$, traced by [C II] and CO across the analyzed SMC regions, as function of the hydrogen column density traced only by [C II] $N(H_2)_{[C\,ii]}$ (See errorbar values in Table 5.3.1). On average, [C II] accounts for about $\sim (77 \pm 4)\%$ (*purple line and shaded region*) of the total $N(H_2)$, demonstrating that the bulk of the molecular gas is found in the "CO-dark" phase. This highlights the dominant role of [C II] as a tracer of molecular gas in low-metallicity environments such as the SMC.The color coding indicates the star formation rate surface density, $\log(\Sigma_{\text{SFR}})$, in units of $[M_\odot\ \text{yr}^{-1}\ \text{kpc}^{-2}]$.

conversion factor $X_{\mathrm{CO+CO_{dark}}} = 7.9 \times 10^{20}$ cm^{-2}(K km s^{-1})$^{-1}$. The Galactic conversion factor is typically calibrated for the CO(1–0) transition. Assuming a line ratio R_{21} =CO(2–1)/CO(1–0)~ 1 for the SMC (Rubio et al. 1996), our result is 4 times larger than the canonical Galactic conversion factor ($X_{\mathrm{CO,MW}} \sim 2 \times 10^{20}$ cm^{-2}(K km s^{-1})$^{-1}$) (Bolatto et al., 2008) reflecting the reduced CO abundance and enhanced CO–faint molecular gas expected in metal-poor environments.

Previous studies have shown that the CO-to-H_2 conversion factor in the SMC is significantly larger than in the Milky Way, although the exact value depends strongly on the method and spatial scale considered. Early observations of molecular clouds in the SMC by Rubio et al. (1996) already suggested an elevated conversion factor relative to the Galactic value, with estimates of $X_{\mathrm{CO}} \sim (1-5) \times 10^{21}$ cm^{-2} (K km s^{-1})$^{-1}$, reflecting the reduced CO brightness in low-metallicity environments. Using virial mass estimates of resolved molecular clouds in the N83/N84 complex, Bolatto et al. (2003) derived a somewhat smaller value of $X_{\mathrm{CO}} \approx (4-7) \times 10^{20}$ cm^{-2} (K km s^{-1})$^{-1}$, a few times larger than the canonical Galactic factor, indicating that CO still traces the densest cloud cores. In contrast, dust-based analyzes that account for the total molecular reservoir, including CO–faint gas, yield significantly larger values across the SMC. for example, Leroy et al. (2007) reported $X_{\mathrm{CO}} \sim (6-13) \times 10^{21}$ cm^{-2} (K km s^{-1})$^{-1}$. Bot et al. (2007) compared the virial masses and dust estimations of the molecular masses, finding that the virial masses are systematically larger (twice on average) than mass estimates from millimeter dust emission. More recent studies combining [C II], [C I], and CO observations have further demonstrated that a substantial fraction of the molecular gas in low-metallicity systems is CO-dark, leading to effectively larger conversion factors when the total H_2 mass is considered (e.g., Pineda et al. (2017), who found $X_{\mathrm{CO}} \sim 10^{21} - 10^{22}$ cm^{-2} (K km s^{-1})$^{-1}$ depending on the region).

5.4 N83-R2, N83-R4 and SWDarkPeak-R7

The tracing of the total molecular gas content in the SMC is assessed mainly through the [C II] 158 μm emission of the selected regions, so we can not carry this examination in N83-R4, since there is no detection of [C II] in the central pixel of the SOFIA/upGREAT array. To perform the linear decomposition of the [C II]

158 μm emission line described in section 4.1, it is necessary to have spectra with at least S/N $\geq$ 10. And since the kinematic intensity peak of CO emission line in N83- R2 is shifted from that of [C II] by $\Delta v \approx 4$ [km s^{-1}], which is out of our tolerance range, and the CO(2-1) spectrum of the SWDarkPeak has a S/N$\approx$ 4.6, we do not perform a further analysis for these regions to maintain the relevance of the results.

5.5 The interesting case of SWDarkPeak

The SWDarkPeak region was found in the dust-based mapping of molecular gas in the SMC by Bolatto et al. (2011) and Jameson et al. (2016) as a likely molecular peak (based on its high dust-to-[H I] ratio) with no known CO emission. Later CO mapping reported by Jameson et al. (2018) detected faint CO emission within the velocity range $\sim$ 137-160 km s^{-1}, and measured and high [C II]/CO ratios. The nature of the SWDarkPeak region makes it an ideal laboratory to study the transition between CO-dark and CO-bright molecular gas. In contrast to other SMC regions, SWDarkPeak shows no associated bright Hα emission, indicating a lack of significant massive star formation and suggesting that the observed [C II] emission arises primarily from photodissociation regions associated with diffuse or weakly shielded molecular gas.

We observed the neutral atomic carbon fine structure transition [CI] (^{3}P$_1$$-^{3}P_0$) at 492.1607 GHz in the SWDarkPeak with APEX as part of project C-0116.F-9708C-2025 (PI: Rodriguez-Ambler) using the nFLASH460 receiver. The [C I](1-0) spectrum line at 492 GHz was obtained in October 2025 with an rms = 0.1 K and a velocity resolution of $\Delta V = 0.4$ km s^{-1}.

We use this low-metallicity region to investigate the impact of PDR conditions on the ability of CO to trace molecular gas. In Fig. 5.5.1, we present the newly acquired [C I] spectrum ($S/N \sim 7$), together with the existing [H I] CO, and [C II] data. Thanks to the high spectral resolution of our observations, we identify two distinct kinematic components along the line of sight toward SWDarkPeak: SWDarkPeak-A (dashed black line) and SWDarkPeak-B (dotted black line). The strong [C II] emission detected at $\sim$ 140 km s^{-1}, which lacks a corresponding [C I] and strong CO counterpart, most likely arises from a CO-dark molecular phase in which hydrogen is predominantly molecular while carbon remains ionized

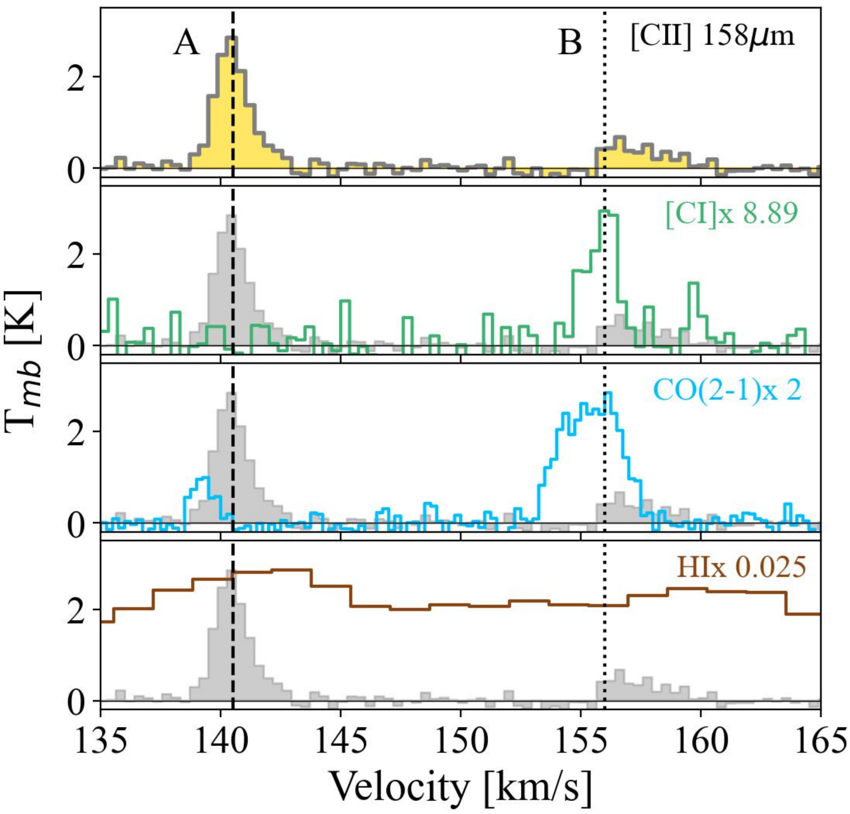

Figure 5.5.1: Spectral emission for the SWDarkPeak region in [C II] (*gold*), [C I] (*green*), CO(2-1) (*light blue*) and [H I](*brown*), normaand the dotted black line indicated the SWDarkPeak-A and SWDarkPeak-B component, respectively.

Table 5.5.1: Carbon phase ratios for the 2 kinematic components along the LOS in the SWDarkPeak region.

Component	$I_{CO}/I_{[CII],mol}$	$I_{[CI]}/I_{[CII],mol}$	$I_{[CI]}/I_{CO}$
SWDarkPeak-A	0.12	-	-
SWDarkPeak-B	3.6	0.46	0.13

due to reduced dust shielding in the low-metallicity environment (Wolfire et al. 2010; Bolatto et al. 2013; Pineda et al. 2013). In contrast, the CO(2-1) and [C I] emission detected at ~ 156 km s^{-1} trace a more shielded molecular component in which carbon has largely transitioned to neutral and molecular (CO) form.

To probe the nature of these two kinematic components, we use our estimates of the molecular gas contribution to the [C II] 158 μm emission ($\overline{f}_{mol} \approx 0.8$; see Figure 5.2.1) to derive the corresponding molecular hydrogen column densities traced by [C II] and CO. For the SWDarkPeak-A component ($v \sim 140$ km s^{-1}), we obtain $N(\mathrm{H_2})_{[\mathrm{C\,II}]} = (1.7 \pm 0.4) \times 10^{21}$ [cm^{-2}] and $N(\mathrm{H_2})_{\mathrm{CO}} = (1.0 \pm 1.7) \times 10^{20}$ cm^{-2}, implying a CO-dark molecular gas fraction of $f_{\mathrm{CO-dark}} = 0.9$. In contrast, for the SWDarkPeak-B component ($v \sim 156$ km s^{-1}), we measure $N(\mathrm{H_2})_{[\mathrm{C\,II}]} = (5.0 \pm 0.1) \times 10^{20}$ cm^{-2} and $N(\mathrm{H_2})_{\mathrm{CO}} = (8.3 \pm 0.6) \times 10^{20}$ cm^{-2}, corresponding to $f_{\mathrm{CO-dark}} = 0.4$. These results suggest that the SWDarkPeak line of sight intercepts two physically distinct molecular environments: a CO-dark molecular component traced primarily by [C II] emission at ~ 140 km s^{-1} and a more shielded molecular cloud traced by CO and [C I] at ~ 156 km s^{-1}.

The simultaneous detection of [C II], [C I], and CO toward the SWDarkPeak-B component further allows us to probe the carbon phase balance within the molecular gas. We compare the integrated line intensities of the three tracers and derive the ratios $I_{\mathrm{CO}}/I_{[\mathrm{C\,II}],mol}$, $I_{[\mathrm{C\,I}]}/I_{[\mathrm{C\,II}],mol}$ and $I_{[\mathrm{C\,I}]}/I_{\mathrm{CO}}$ for each velocity component. As shown in Table 5.5.1, the SWDarkPeak-A component exhibits a very low $I_{\mathrm{CO}}/I_{[\mathrm{C\,II}],mol}$ ratio together with an undetected [C I] counterpart, indicating that the carbon reservoir is dominated by ionized carbon. In contrast, the SWDarkPeak-B component shows detected [C I] and CO emission, suggesting that carbon has largely transitioned from C^+ to neutral and, mostly, molecular forms. This behavior follows the classical stratification expected in photodissociation regions, where the dominant carbon phase evolves from C^+ to C^0 and finally to CO with increasing shielding (Tielens and Hollenbach (1985);

Hollenbach and Tielens (1999)).

Chapter 6

Conclusion

Using velocity-resolved SOFIA/GREAT and upGREAT [C II] 158 μm, APEX, and ATCA+Parkes [H I] 21 cm observations, we decomposed the [C II] emission in several regions of the Small Magellanic Cloud into atomic and molecular components following the approach of Tarantino et al. (2021). On average, $(81 \pm 1)\%$ of the [C II] luminosity arises from the molecular phase, while $(15 \pm 1)\%$ is associated with atomic gas, confirming that [C II] predominantly traces molecular gas in low-metallicity environments (e.g.,Requena-Torres et al. (2016); Langer et al. (2014); Pineda et al. (2014)). The residuals of the [C II] decomposition are mostly positive, indicating that the linear fitting approach tends to underestimate the [C II] emission fractions, particularly from the molecular component. A small additional contribution ($\lesssim$ 4%) may arise from ionized gas, as suggested by Herrera-Camus et al. (2016) and Croxall et al. (2017). Complementary [NII] observations would be necessary to quantify this contribution in detail for the SMC.

Converting the decomposed [C II]emission into column densities using the approach described in Section 4.4.1, we find that the [C II] traced H_2 accounts for roughly $(77 \pm 4)\%$ of the total molecular gas column density, with the remaining $\sim 20\%$ traced by CO. This demonstrates that the bulk of the molecular gas in the SMC is CO-faint, consistent with results obtained for other low-metallicity systems (e.g., Jameson et al. (2018); Madden et al. (2020)). Consequently, CO tracers would underestimate the total H_2 mass by a factor of about four, in agreement with PDR model predictions for low-Z environments Wolfire et al. (2010); Hollenbach et al.

(2012). Thus, we propose a new CO-to-H_2 conversion factor $X_{CO} \approx 7.94 \times 10^{21}$ cm^{-2} (K km $s^{-1})^{-1}$. This value is 4 times larger than the canonical Galactic conversion factor.

We find no significant correlation between the CO-dark fraction, $N(H_2)_{[C\,ii]}/N(H_2)_{total}$, and either the total molecular column density or the star formation rate surface density. This suggests that the abundance of CO-faint gas is not primarily driven by local density or star formation, but instead by the efficiency of dust and gas shielding against the FUV radiation field, which scales with metallicity (e.g., Bolatto et al. (2013); Leroy et al. (2011); Okada et al. (2019)). Future work will explore the spatially resolved spectroscopic data from the *Local Volume Mapper* (LVM) of SDSS-V Kollmeier et al. (2019) to investigate possible metallicity gradients across the SMC and their effect on the [C II]/CO relation.

Our study demonstrates that [C II] is the dominant tracer of molecular gas in the SMC (77%) and likely in other metal-poor systems. The CO-dark molecular phase represents an extended, stable, and significant component of the low-metallicity interstellar medium that is not primarily driven by stellar feedback, but rather by chemical processes. This provides a crucial reference for interpreting [C II] emission in unresolved galaxies at both local and high redshift (e.g., Cormier et al. (2019); Okada et al. (2019)). However, caution is required when extrapolating these results to high-redshift galaxies, since the physical conditions in the early Universe, such as higher gas surface densities and star formation rates, stronger radiation fields, and potentially different ISM distributions, can significantly alter the relative contributions of atomic, molecular, and ionized gas to the [C II] emission.

Bibliography

Aniano, G., Draine, B. T., Calzetti, D., Dale, D. A., Engelbracht, C. W., Gordon, K. D., Hunt, L. K., et al. (2012). Modeling dust emission in nearby galaxies with spitzer and herschel data. ApJ, 756:138.

Aniano, G., Draine, B. T., Hunt, L. K., Sandstrom, K., Calzetti, D., Kennicutt, R. C., Dale, D. A., et al. (2020). Comprehensive dust modeling in nearby galaxies. ApJ, 889:150.

Bakes, E. L. O. and Tielens, A. G. G. M. (1994). The photoelectric heating mechanism for very small graphite grains and polyclic aromatic hydrocarbons. ApJ, 427:822.

Bolatto, A. D., A., L., P., I. F., and M., J. J. (2003). Unusual co line ratios and kinematics in the n83/n84 region of the small magellanic cloud. In ApJ, volume 595, page 167.

Bolatto, A. D., Leroy, A. K., Jameson, K., Ostriker, E., Gordon, K., Lawton, B., Stanimirović, S., Israel, F. P., Madden, S. C., Hony, S., Sandstrom, K. M., Bot, C., Rubio, M., Winkler, P. F., Roman-Duval, J., van Loon, J. T., Oliveira, J. M., and Indebetouw, R. (2011). The State of the Gas and the Relation between Gas and Star Formation at Low Metallicity: The Small Magellanic Cloud. , 741(1):12.

Bolatto, A. D., Leroy, A. K., Rosolowsky, E., Walter, F., and Blitz, L. (2008). The resolved properties of extragalactic giant molecular clouds. In IAU Symposium, volume 255, page 274.

Bolatto, A. D., Wolfire, M., and Leroy, A. K. (2013). The co-to-h2 conversion factor. ARA&A, 51:207.

Bot, C., Boulange, F., Rubio, M., and Rantakyro, F. (2007). Millimeter dust continuum emission revealing the true mass of giant molecular clouds in the small magellanic cloud. A&A, 471:103.

Calzetti, D., Kennicutt, R. C., Engelbracht, C. W., Leitherer, C., Draine, B. T., Kewley, L., Moustakas, J., Sosey, M., Dale, D. A., Gordon, K. D., Helou, G. X., Hollenbach, D. J., Armus, L., Bendo, G., Bot, C., Buckalew, B., Jarrett, T., Li, A., Meyer, M., Murphy, E. J., Prescott, M., Regan, M. W., Rieke, G. H., Roussel, H., Sheth, K., Smith, J. D. T., Thornley, M. D., and Walter, F.

(2007). The Calibration of Mid-Infrared Star Formation Rate Indicators. ApJ, 666(2):870.

Carilli, C. L. and Walter, F. (2013). Cool gas in high-redshift galaxies. ARA&A, 51:105.

Chastenet, J., Sandstrom, K., Leroy, A. K., Bot, C., Chiang, I.-D., Chown, R., Gordon, K. D., et al. (2025). The dustpedia project: Fir and submillimeter dust emission in nearby galaxies. ApJS, 276:2.

Cormier, D., Abel, N. P., Hony, S., Lebouteiller, V., Madden, S. C., Polles, F. L., Galliano, F., et al. (2019). The herschel dwarf galaxy survey ii: The origin of [cii] emission in low-metallicity environments. A&A, 626:A23.

Crawford, M. K., Genzel, R., Townes, C. H., and Watson, D. M. (1985). Far-infrared spectra of galactic star-forming regions. ApJ, 291:755.

Croxall, K. V., Smith, J. D., Pellegrini, E., Groves, B., Bolatto, A., Herrera-Camus, R., Sandstrom, K. M., et al. (2017). The kingfish [cii] survey: Tracing the phases of the ism. ApJ, 845:96.

Draine, B. T., Dale, D. A., Bendo, G., Gordon, K. D., Smith, J. D. T., Armus, L., Engelbracht, C. W., et al. (2007). Dust emission in the sings galaxy sample. ApJ, 663:866.

Draine, B. T. and Li, A. (2007). Infrared emission from interstellar dust. iv. the silicate-graphite-pah model. ApJ, 657:810.

Galametz, M., Kennicutt, R. C., Calzetti, D., Aniano, G., Draine, B. T., Boquien, M., Brandl, B., et al. (2013). The dust properties of star-forming galaxies from the kingfish survey. MNRAS, 431:1956.

Gordon, K. D., Roman-Duval, J., Bot, C., Meixner, M., Babler, B., Bernard, J.-P., Bolatto, A., et al. (2014). Dust and gas in the small magellanic cloud. ApJ, 797:85.

Grenier, I. A., Casandjian, J.-M., and Terrier, R. (2005). Unveiling Extensive Clouds of Dark Gas in the Solar Neighborhood. Science, 307(5713):1292.

Güsten, R., Nyman, L. Å., Schilke, P., Menten, K., Cesarsky, C., and Booth, R. (2006). The atacama pathfinder experiment (apex) telescope. A&A, 454:L13.

Hao, C.-N., Kennicutt, R. C., Johnson, B. D., Calzetti, D., Dale, D. A., and Moustakas, J. (2011). Dust-corrected star formation rates of nearby galaxies. ApJ, 741:124.

Herrera-Camus, R., Bolatto, A., Smith, J. D., Draine, B., Pellegrini, E., Wolfire, M., Croxall, K., et al. (2016). The origin of [cii] emission in nearby galaxies. ApJ, 826:175.

Herrera-Camus, R., Bolatto, A. D., Wolfire, M. G., Smith, J. D., Croxall, K. V., Kennicutt, R. C., Calzetti, D., et al. (2015). The [cii] deficit in local luminous infrared galaxies. ApJ, 800:1.

Herrera-Camus, R., Sturm, E., Graciá-Carpio, J., Lutz, D., Contursi, A., Veilleux, S., Fischer, J., et al. (2018). Far-infrared line diagnostics of galactic winds. ApJ, 861:95.

Heyminck, S., Graf, U. U., Güsten, R., Stutzki, J., Hübers, H.-W., and Hartogh, P. (2012). Great: The german receiver for astronomy at terahertz frequencies. A&A, 542:L1.

Hollenbach, D., Kaufman, M. J., Neufeld, D., Wolfire, M., and Goicoechea, J. R. (2012). Photodissociation regions in the interstellar medium. ApJ, 754:105.

Hollenbach, D. J. and Tielens, A. G. G. M. (1999). Photodissociation regions in the interstellar medium of galaxies. Reviews of Modern Physics, 71(1):173.

Israel, F. P. and Maloney, P. R. (2011). Co and [cii] emission in the small magellanic cloud. A&A, 531:A19.

Israel F. P., Maloney P. R., G. N. H. F. M. S. C. P. A. S. G. J. (1996). C+ emission from the magellanic clouds. i. the bright h ii region complexes n159 and n160. ApJ, 465:738.

Jameson, K. E., Bolatto, A. D., Leroy, A. K., Meixner, M., Roman-Duval, J., Gordon, K., Hughes, A., Israel, F. P., Rubio, M., Indebetouw, R., Madden, S. C., Bot, C., Hony, S., Cormier, D., Pellegrini, E. W., Galametz, M., and Sonneborn, G. (2016). The Relationship Between Molecular Gas, H I, and Star Formation in the Low-mass, Low-metallicity Magellanic Clouds. , 825(1):12.

Jameson, K. E., Bolatto, A. D., Wolfire, M., Warren, S. R., Herrera-Camus, R., Croxall, K., Pellegrini, E., et al. (2018). The origin of [cii] emission in star-forming regions. ApJ, 853:111.

Kaufman, M. J., Wolfire, M. G., and Hollenbach, D. J. (2006). The impact of metallicity on pdrs. ApJ, 644:283.

Kaufman, M. J., Wolfire, M. G., Hollenbach, D. J., and Luhman, M. L. (1999). Far-infrared and submillimeter emission from photodissociation regions. ApJ, 527:795.

Kennicutt, R. C. and Evans, N. J. (2012). Star formation in the milky way and nearby galaxies. ARA&A, 50:531.

Kennicutt, Jr., R. C. (1998). The global schmidt law in star-forming galaxies. ApJ, 498:541.

Kennicutt, Jr., R. C., Hao, C.-N., Calzetti, D., Moustakas, J., Dale, D. A., Bendo, G., Engelbracht, C. W., Johnson, B. D., and Lee, J. C. (2009). Dust-corrected Star Formation Rates of Galaxies. I. Combinations of Hα and Infrared Tracers. , 703(2):1672–1695.

Kollmeier, J., Anderson, S. F., Blanc, G. A., Blanton, M. R., Covey, K. R., Crane, J., Drory, N., et al. (2019). Sdss-v: Pioneering panoptic spectroscopy. BAAS, 51:274.

Kroupa, P. (2001). On the variation of the initial mass function. MNRAS, 322:231.

Langer, W. D., Velusamy, T., Pineda, J. L., Willacy, K., and Goldsmith, P. F. (2014). The co-dark h2 gas component of the milky way. A&A, 561:A122.

Lebouteiller, V., Cormier, D., Madden, S. C., Galliano, F., Indebetouw, R., Abel, N., Sauvage, M., et al. (2012). The physical conditions of the ism in dwarf galaxies. A&A, 548:A91.

Lee, C., Leroy, A. K., Schnee, S., Wong, T., Bolatto, A. D., Indebetouw, R., and Rubio, M. (2015). Molecular cloud properties in the magellanic clouds. MNRAS, 450:2708.

Leroy, A., Bolatto, A., Stanimirovic, S., Mizuno, N., Israel, F., and Bot, C. (2007). The Spitzer Survey of the Small Magellanic Cloud: Far-Infrared Emission and Cold Gas in the Small Magellanic Cloud. , 658(2):1027–1046.

Leroy, A. K., Bolatto, A., Gordon, K., Sandstrom, K., Gratier, P., Rosolowsky, E., Engelbracht, C. W., et al. (2011). The co-to-h2 conversion factor from dust and gas in nearby galaxies. ApJ, 737:12.

Leroy, A. K., Hughes, A., Schruba, A., Rosolowsky, E., Blanc, G. A., Bolatto, A. D., Colombo, D., et al. (2016). Cloud-scale molecular gas properties in nearby galaxies. ApJ, 831:16.

Li, A. and Draine, B. T. (2002). Infrared emission from interstellar dust. iii. the small magellanic cloud. ApJ, 576:792.

Li, A. and Draine, B. T. (2002c). Infrared Emission from Interstellar Dust. III. The Small Magellanic Cloud. , 576(2):762–772.

Madden, S. C., Cormier, D., Hony, S., Lebouteiller, V., Abel, N., Galametz, M., De Looze, I., et al. (2020). The herschel dwarf galaxy survey: Co-dark gas and [cii] cooling. A&A, 643:A141.

Meixner, M., Panuzzo, P., Roman-Duval, J., Engelbracht, C., Babler, B., Seale, J., Hony, S., et al. (2013). The heritage herschel survey of the magellanic clouds. AJ, 146:62.

Muller E., Ott J., H. A. P. J. W. T. M. N. K. A. M. Y. F. Y. O. T. R. M. e. a. (2010). Characterizing the low-mass molecular component in the northern small magellanic cloud. ApJ, 712:1248.

Okada, Y., Güsten, R., Requena-Torres, M. A., Röllig, M., Stutzki, J., Graf, U. U., and Hughes, A. (2019). The [cii] and co emission in the small magellanic cloud. A&A, 621:A62.

Okada, Y., Requena-Torres, M. A., Güsten, R., Stutzki, J., Wiesemeyer, H., Pütz, P., and Ricken, O. (2015). Velocity-resolved [cii] emission in the lmc and smc. A&A, 580:A54.

P., I. F. (1997). H_2 and its relation to co in the lmc and other magellanic irregular galaxies. A&A, 328:471.

Pineda, J. L., Langer, W. D., and Goldsmith, P. F. (2014). The co-dark molecular gas in the milky way. A&A, 570:A121.

Pineda, J. L., Langer, W. D., Goldsmith, P. F., Horiuchi, S., Kuiper, T. B. H., Muller, E., Hughes, A., et al. (2017). Characterizing the transition from diffuse atomic to dense molecular clouds in the magellanic clouds with [c ii], [c i], and co. ApJ, 839:107.

Pineda, J. L., Langer, W. D., Velusamy, T., and Goldsmith, P. F. (2013). The transition from atomic to molecular gas in the milky way. A&A, 554:A103.

Requena-Torres, M. A., Israel, F. P., Okada, Y., Güsten, R., Stutzki, J., Risacher, C., Simon, R., et al. (2016). Velocity-resolved [cii] observations in the magellanic clouds. A&A, 589:A28.

Risacher, C., Güsten, R., Stutzki, J., Hübers, H.-W., Aladro, R., Bell, A., Buchbender, C., et al. (2018). upgreat: Upgrade of the german receiver for astronomy at terahertz frequencies. JAI, 7:1840014.

Rubio, M., J., L., F., B., S., B. R., de Graauw T., G. G., and et al., I. F. P. (1996). Results of the eso-sest key programme: Co in the magellanic clouds. v. further co observations of the small magellanic cloud. A&AS, 118:263.

Rubio M., Elmegreen B. G., H. D. A. B. E. C. J. R. C. P. (2015). Dense cloud cores revealed by co in the low metallicity dwarf galaxy wlm. Nature, 525:218.

Saldaño, H. P., Rubio, M., Bolatto, A. D., Verdugo, C., Jameson, K. E., and Leroy, A. K. (2023). Apex co(2–1) survey of the small magellanic cloud. A&A, 672:A153.

Sandstrom, K. M., Bolatto, A. D., Draine, B. T., Bot, C., and Stanimirović, S. (2010). The co-to-h2 conversion factor in the small magellanic cloud. ApJ, 715:701.

Sauvage, M., Thuan, T. X., and Vigroux, L. (1990). The effects of stellar age and metallicity on the infrared emission in the Magellanic clouds. A&A, 237:296.

Schwering, P. B. W. and Israel, F. P. (1990). Atlas and catalogue of infrared sources in the Magellanic Clouds. Springer Nature.

Shetty, R., Glover, S. C., Dullemond, C. P., and Klessen, R. S. (2011). Modeling co emission in molecular clouds: The co-to-h2 conversion factor. MNRAS, 412:1686.

Stanimirović, S., L., S.-S., and A., J. P. (2004). A new look at the kinematics of neutral hydrogen in the small magellanic cloud. ApJ, 604:176.

Stanimirović, S., Staveley-Smith, L., Dickey, J. M., Sault, R. J., and Snowden, S. L. (1999). The large-scale hi structure of the small magellanic cloud. MNRAS, 302:417.

Stanimirović, S., Staveley-Smith, L., van der Hulst, J. M., Bontekoe, T. R., Kester, D. J. M., and Jones, P. A. (2000). Cool dust and gas in the small magellanic cloud. MNRAS, 315:791.

Sun, J., Leroy, A. K., Schruba, A., Rosolowsky, E., Hughes, A., Kruijssen, J. M. D., Meidt, S., et al. (2018). Resolved star formation relations in nearby galaxies. ApJ, 860:172.

Tarantino, E., Bolatto, A. D., Herrera-Camus, R., Harris, A. I., Wolfire, M., Buchbender, C., Croxall, K. V., et al. (2021). The velocity decomposition of [cii] in local galaxies. ApJ, 915:92.

Tielens, A. G. G. M. and Hollenbach, D. (1985). Photodissociation regions. ii. a model for the orion photodissociation region. ApJ, 291:747.

Vassilev, V., Meledin, D., Lapkin, I., Belitsky, V., Nyström, O., Henke, D., Pavolotsky, A., et al. (2008). The apex swedish heterodyne facility instrument (shfi). A&A, 490:1157.

Wiesenfeld, L. and Goldsmith, P. F. (2014). Collisional excitation of c+ by atomic and molecular hydrogen. ApJ, 780:183.

Winkler, P. F., Points, S. D., Smith, R. C., and Team, M. (2015). The magellanic cloud emission line survey (mcels). In Astronomical Society of the Pacific Conference Series, volume 491, page 343.

Wolfire, M. G., Hollenbach, D., and McKee, C. F. (2010). The neutral atomic phases of the interstellar medium. ApJ, 716:1191.

Appendix A

A1 Complementary Data

A1.1 Hα emission map

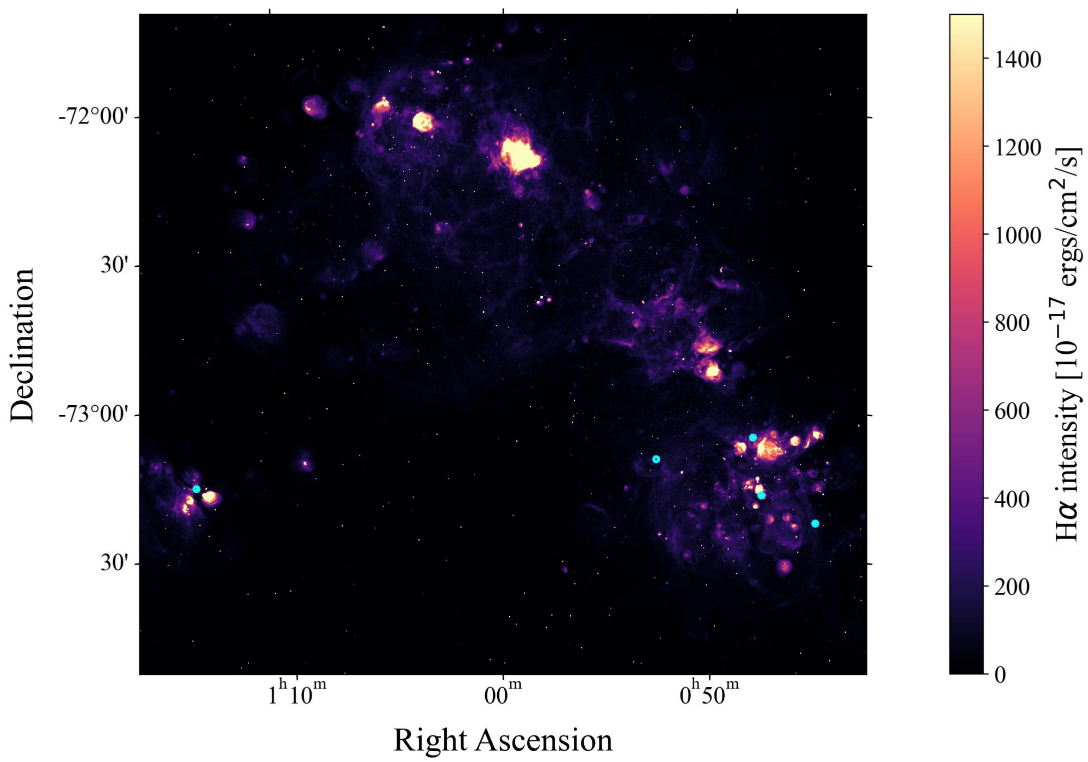

Figure A1.1: SMC continuum substracted mosaic Hα emission map, from Winkler et al. (2015), with [10^{-17} erg/cm^2/s] units. The selected SMC targets are pointed with cyan dots.

A1.2 Draine & Li 2007 mixture maps

We extracted the DL07 SMC mixture maps from Chastenet et al. (2025), where they obtained the average radiation field $\langle U \rangle$ and the surface density map ΣM_{dust}, along with other dust parameters that were not considered in this estimation. In Figure A1.2 we see that the higher levels of the radiation field avoid our targets, meanwhile in Figure A1.3 is shown that our selected SMC regions overlap with the dust mass peaks. The methodology described in Section 4.1.1 was applied to compute the total infrared luminosity map predicted by the Draine and Li (2007) model. We find that the total infrared luminosity is structured across the SMC and traces the molecular gas, since its intensity peaks are concentrated in the main star-forming complexes located along the Bar, as shown in Figure A1.4. This map contains all of our SMC targets, except for the SWbarN regions, which were located at an empty pixel (See Figure A1.5)

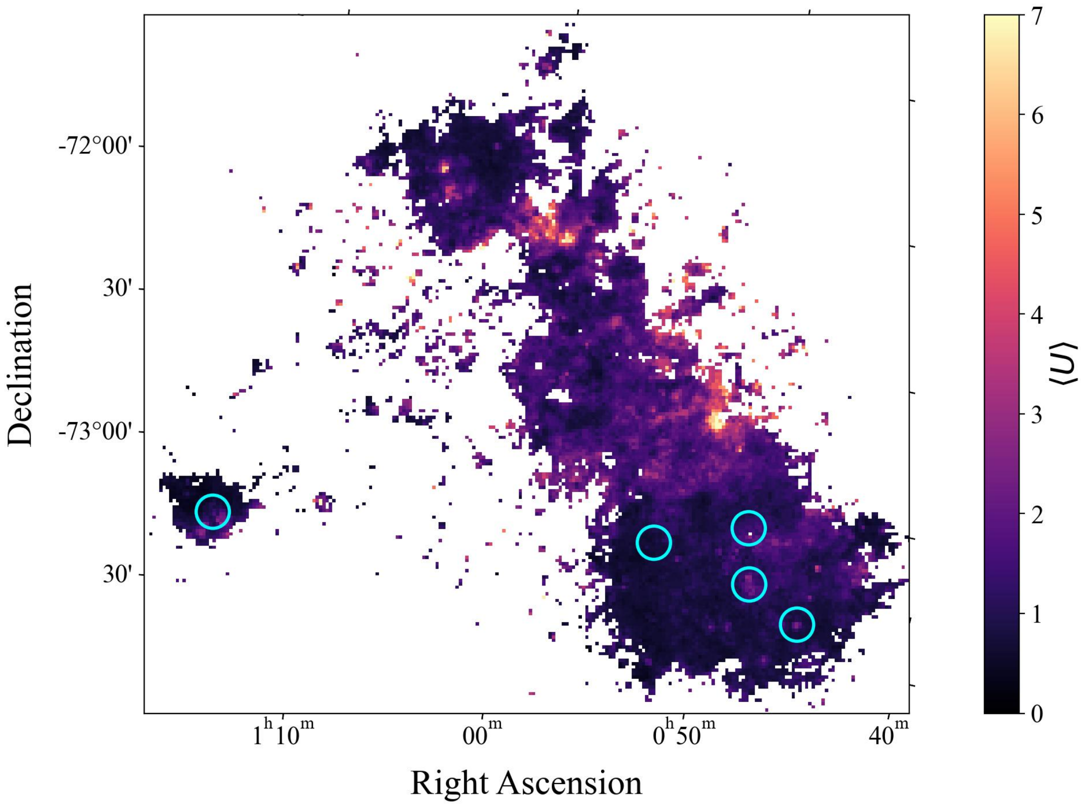

Figure A1.2: Dust mass weighted mean interstellar radiation field from Chastenet et al. (2025) to the SMC. $\langle U \rangle$ is expressed relative to the local Solar neighborhood field ($U = 1$). Higher values, located mainly in the surroundings areas of our selected SMC regions (*cyan circles*), represent regions with strong FUV radiation.

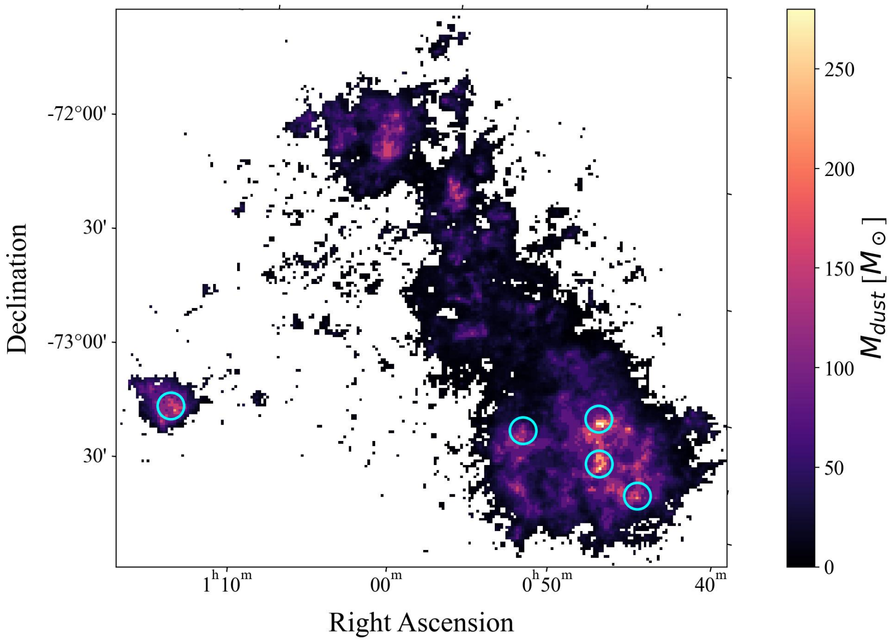

Figure A1.3: Map of the DL07 inferred dust mass per pixel across the SMC from Chastenet et al. (2025) (colorbar in Solar masses). The distribution highlights dust concentrations in the main body and Wing. Blank (*white* and *black*) pixels indicate areas outside the reliable fit region.

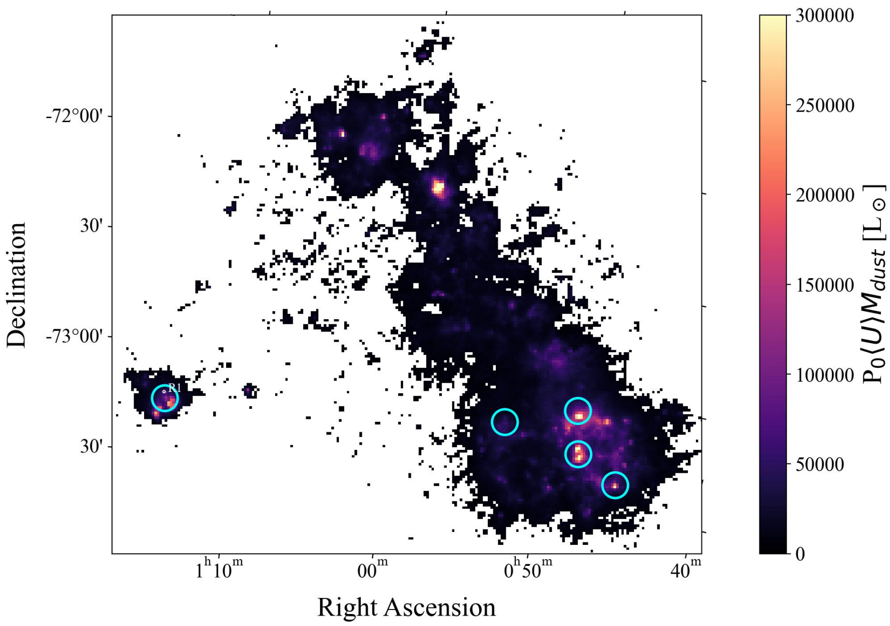

Figure A1.4: Map of dust luminosity per pixel, in solar luminosity units, based on the SMC DL07 mixture results of Chastenet et al. (2025) and the DL07 model of Draine et al. (2007). Our SMC regions are pointed with cyan circles.

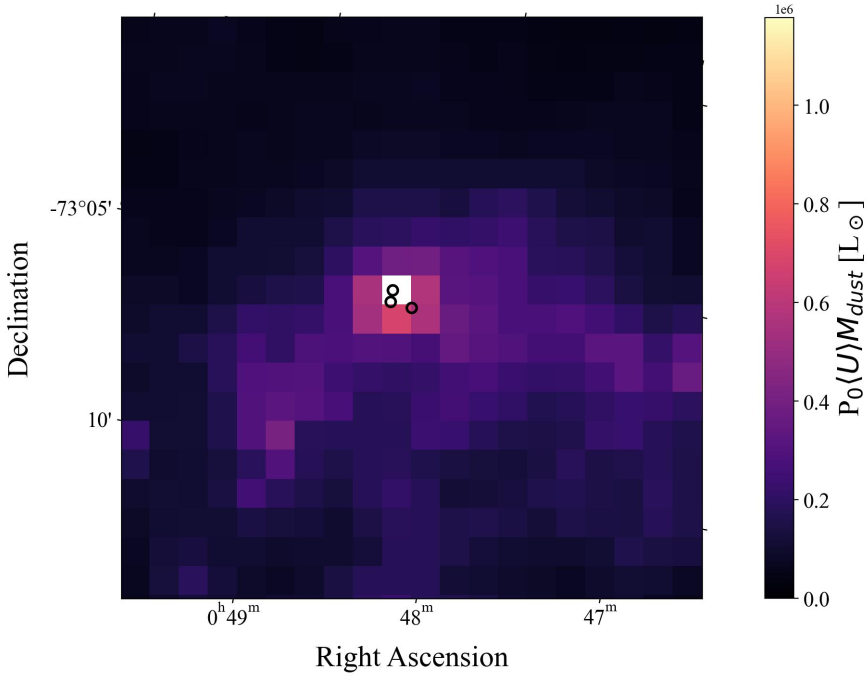

Figure A1.5: Computed DL07 SMC mixture map from Chastenet et al. (2025) where is shown the NaN pixel within the SWbarN regions (*black empty circles.*)

A2 Modeled [C II] emission line profiles

The rebinned spectra of [C II] 158 *μm (yellow)*, CO(2-1) *(light blue)*, which match the HI line profile *(brown)* velocity resolution are shown in this section to provide a full perspective of the discussed results. The HI and CO spectra are normalized to the maximum intensity of the [C II] spectra. The dashed black line corresponds to the decomposed [C II] 158 *μm* emission.

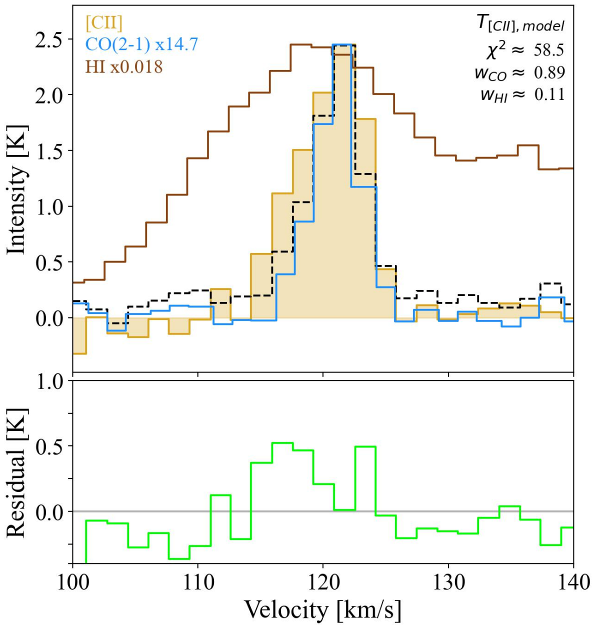

Figure A2.1: N22-R1 modeled [C II] 158 μm emission with linear coefficients $w_{CO} \approx 0.89$ and $w_{HI} \approx 0.11$ and reduced $\chi^2 \approx 58.5$. The residual between the decomposed and the rebinned emission of [C II] is mainly positive.

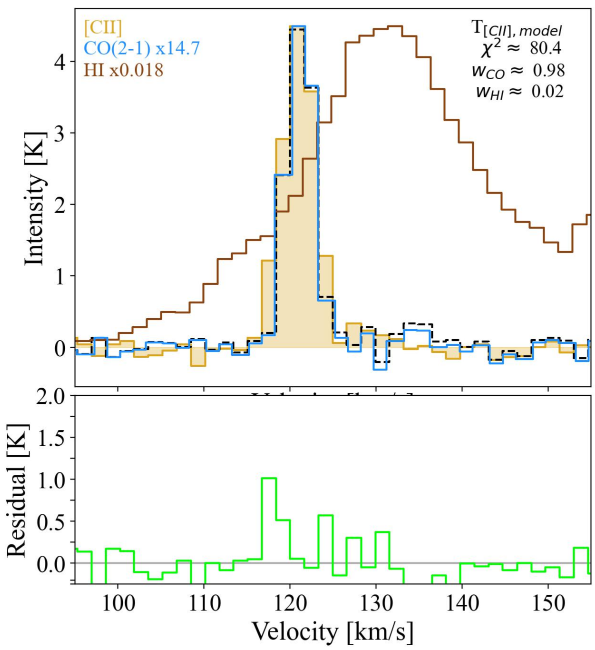

Figure A2.2: N22-R2 modeled [C II] 158 μm emission with linear coefficients $w_{CO} \approx 0.98$ and $w_{HI} \approx 0.02$ and reduced $\chi^2 \approx 80.4$. The residual between the decomposed and the rebinned emission of [C II] is mainly positive.

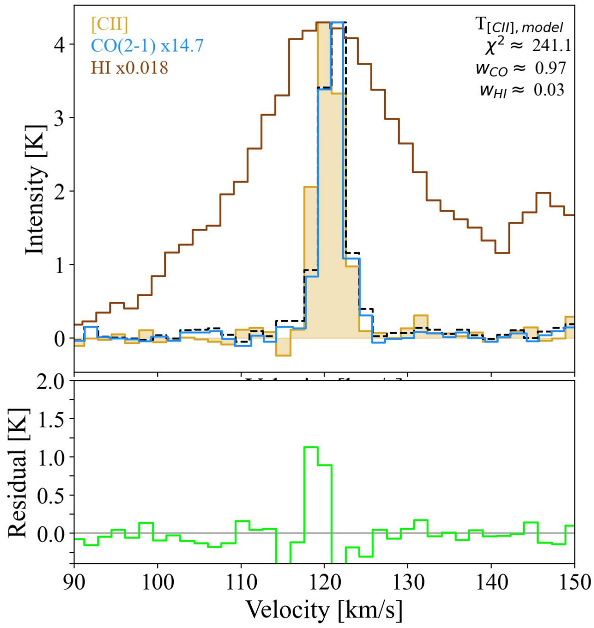

Figure A2.3: N22-R3 modeled [C II] 158 μm emission with linear coefficients $w_{CO} \approx 0.97$ and $w_{HI} \approx 0.03$ and reduced $\chi^2 \approx 241.1$. The residual between the decomposed and the rebinned emission of [C II] is positive, with minor negative contributions.

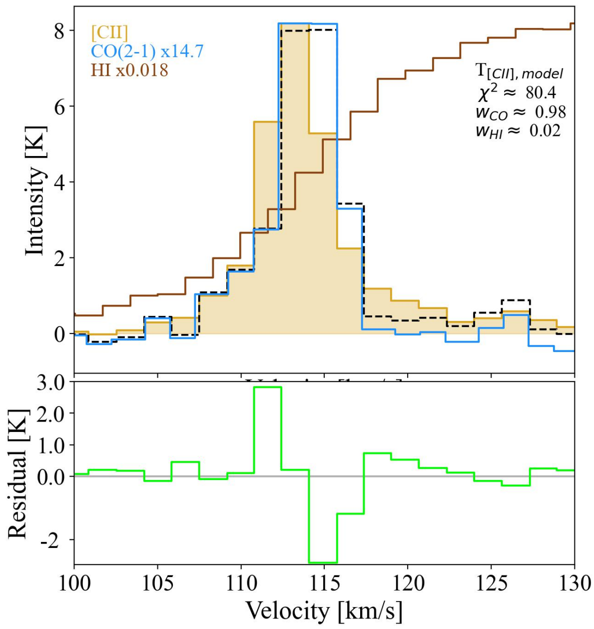

Figure A2.4: SWbarN-R4 modeled [C II] 158 μm emission with linear coefficients $w_{CO} \approx 0.98$ and $w_{HI} \approx 0.02$ and reduced $\chi^2 \approx 80.4$. The residual between the decomposed and the rebinned emission of [C II] is positive with a negative counterpart.

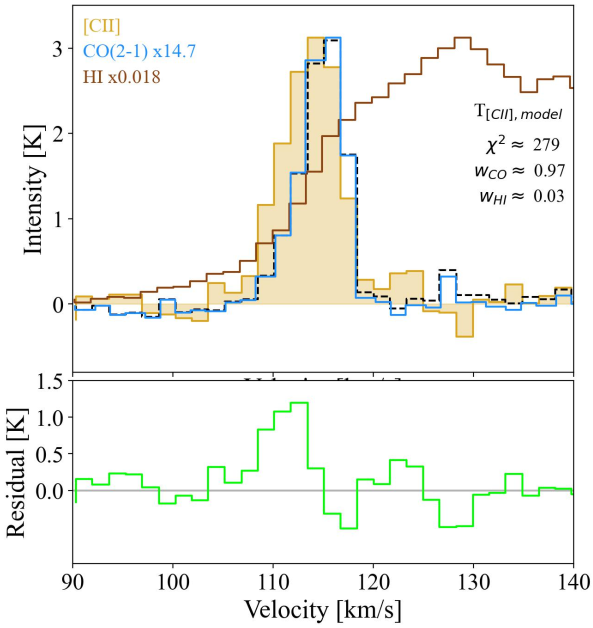

Figure A2.5: SWbarN-R5 modeled [C II] 158 μm emission with linear coefficients $w_{CO} \approx 0.97$ and $w_{HI} \approx 0.03$ and reduced $\chi^2 \approx 279$. The residual between the decomposed and the rebinned emission of [C II] is mainly positive, with a minor negative features.

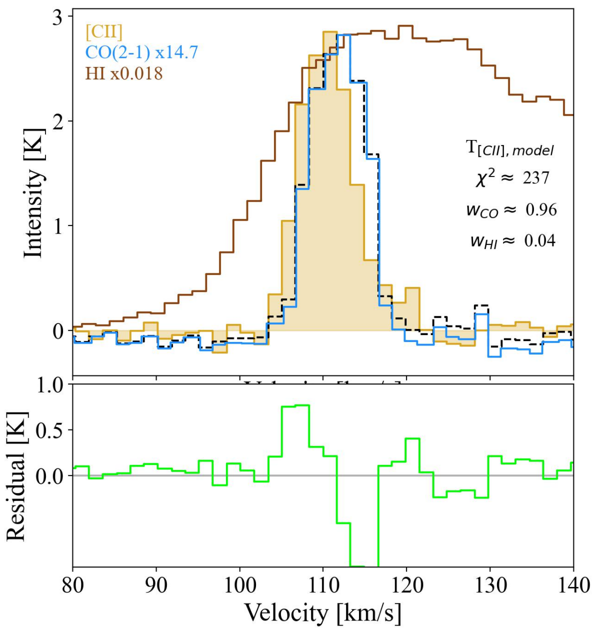

Figure A2.6: SWnarN-R6 modeled [C II] 158 μm emission with linear coefficients $w_{CO} \approx 0.89$ and $w_{HI} \approx 0.11$ and reduced $\chi^2 \approx 58.5$. The residual between the decomposed and the rebinned emission of [C II] is mainly positive, yet it still presents negative atributes.

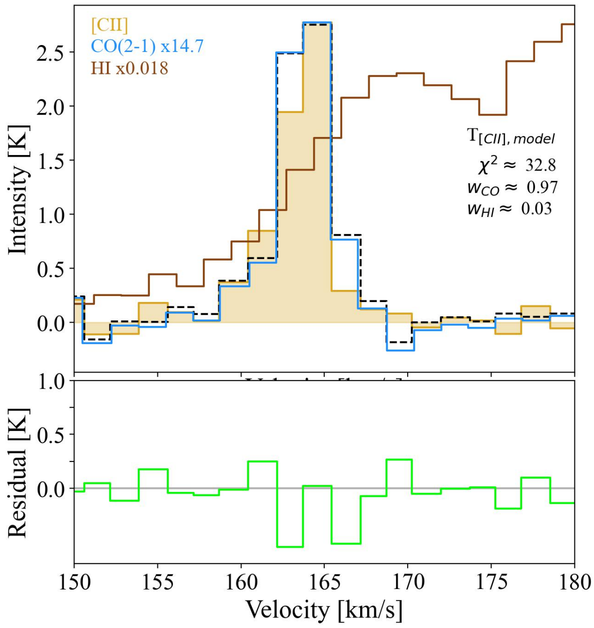

Figure A2.7: N83-R1 modeled [C II] 158 μm emission with linear coefficients $w_{CO} \approx 0.89$ and $w_{HI} \approx 0.11$ and reduced $\chi^2 \approx 58.5$. The residual between the decomposed and the rebinned emission of [C II] is mainly positive.

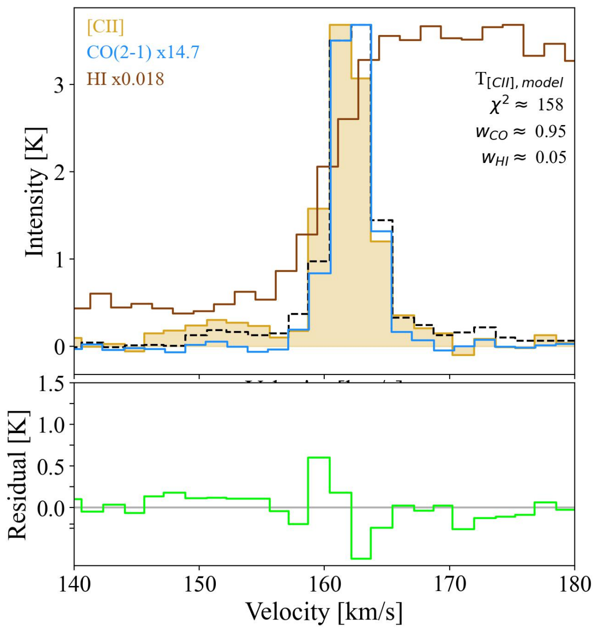

Figure A2.8: N83-R3 modeled [C II] 158 μm emission with linear coefficients $w_{CO} \approx 0.95$ and $w_{HI} \approx 0.05$ and reduced $\chi^2 \approx 158$. The residual between the decomposed and the rebinned emission of [C II] is positive with a negative counterpart.

A3 Spectral lines parameters summary

The integrated line intensity was computed for the rebinned spectra, while the other parameters were obtained from the original velocity resolution of each fitted

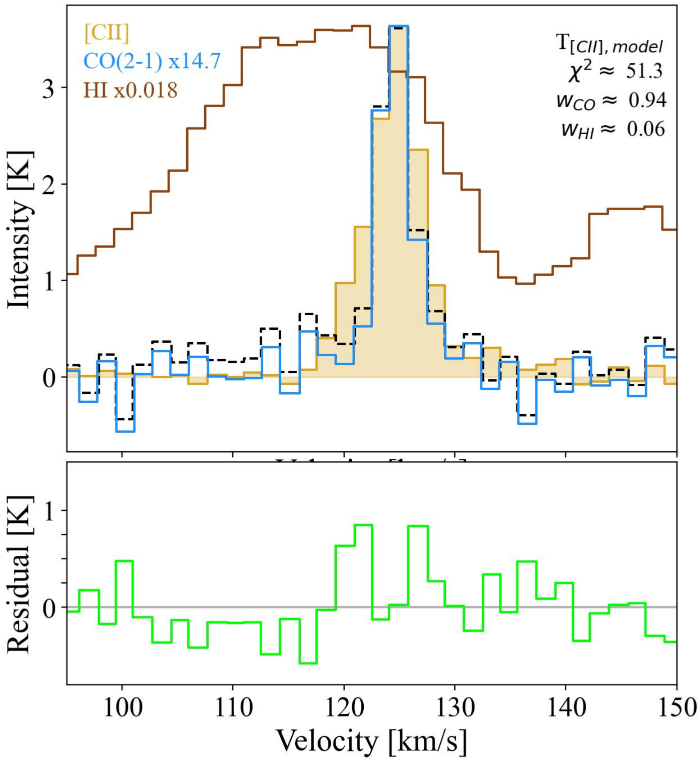

Figure A2.9: SWbarS-R6 modeled [C II] 158 μm emission with linear coefficients $w_{CO} \approx 0.94$ and $w_{HI} \approx 0.06$ and reduced $\chi^2 \approx 51.3$. The residual between the decomposed and the rebinned emission of [C II] is mainly positive.

spectral line. In both cases the CO and [H I] spectra were normalized to the [C II] peak intensity.

Table A3.1: [C II] properties for each SMC region.

Region	v_{peak} [1]	[C II] $FWHM$[2]	$\int I_{[\text{C II}]} dv$ [3]
N83-R1	164.1	2.278	11.20
N83-R2	159.3	5.185	12.52
N83-R3	161.7	3.707	19.63
N83-R4	-	-	-
SWbarS-R5	124.6	9.240	24.76
SWbarS-R6	124.8	4.158	22.87
SWbDarkPeak-R7	140.1	1.249	8.733
N22-R1	119.6	6.566	16.45
N22-R2	120.9	4.554	23.68
N22-R3	120.3	3.645	17.88
SWbarN-R4	114.0	3.711	49.26
SWbarN-R5	113.7	6.681	22.99
SWbarN-R6	111.1	7.138	22.94

Table A3.2: CO properties for each SMC region.

		CO	
Region	$v_{\rm peak}$ [1]	$FWHM$ [2]	$\int I_{\rm CO} dv$ [3]
N83-R1	163.3	1.730	4.92
N83-R2	163.7	2.714	5.72
N83-R3	162.0	3.079	17.35
N83-R4	-	-	-
SWbarS-R5	126.3	6.776	14.25
SWbarS-R6	124.7	3.211	4.480
SWbDarkPeak-R7 139.4	1.028	2.989	
N22-R1	121.3	4.723	3.817
N22-R2	121.2	3.421	7.881
N22-R3	120.3	2.618	11.96
SWbarN-R4	114.9	3.407	15.09
SWbarN-R5	113.3	5.026	20.26
SWbarN-R6	110.3	4.562	15.95

Table A3.3: [H I] properties for each SMC region.

		[H I]	
Region	$v_{\rm peak}$ [1]	$FWHM$ [2]	$\int I_{\rm [HI]} dv$ [3]
N83-R1	182.3	10.39	1822
N83-R2	170.4	12.58	2388
N83-R3	178.0	16.96	2928
N83-R4	-	-	
SWbarS-R5	120.96	22.62	2538
SWbarS-R6	119.4	25.44	2085
SWbDarkPeak-R7	161.6	21.40	5318
N22-R1	118.8	16.33	2182
N22-R2	131.9	24.14	2639
N22-R3	121.4	25.05	1937
SWbarN-R4	126.7	24.84	1907
SWbarN-R5	126.6	24.52	2507
SWbarN-R6	113.5	22.31	1347

[1] Estimated velocity peak position of the spectral line's main gaussian component in km s^{-1}.
[2] Measured line width of the spectral line's main gaussian component in units of km s^{-1}.
[3] Integrated intensity [K km s^{-1}] of the whole line profile.